DARK MATTER DECAYS FROM THE GALACTIC CENTER USING ICECUBE-86

by

JAMES PEPPER

DAWN R. WILLIAMS, COMMITTEE CHAIR
CONOR HENDERSON
WILLIAM KEEL
NOBUCHIKA OKADA
PATRICK TOALE
SU GUPTA

A DISSERTATION

Submitted in partial fulfillment of the requirements
for the degree of Doctor of Philosophy
in the Department of Physics and Astronomy
in the Graduate School of
The University of Alabama

TUSCALOOSA, ALABAMA

2017

ABSTRACT

Most searches for Dark Matter primarily focus on the WIMP paradigm, which predicts dark matter masses in the GeV - 10 TeV range. However, these relatively low energy searches continue to produce null results, possibly suggesting that dark matter is something other than WIMPs. Gravitinos, on the other hand, can satisfy the cosmological constraints on dark matter, and decay with a lifetime orders of magnitude longer than the age of the universe, producing extremely high energy neutrinos. The IceCube Neutrino Observatory has already had success detecting EHE extragalactic neutrinos, and is well suited to search for dark matter in this high energy regime. This analysis sets limits on the gravitino lifetime from the high energy neutrino events observed at IceCube using three possible astrophysical explanations of the neutrino flux. The most conservative limit on the gravitino lifetime using the softest two-body decay mode was found to be $\tau_{DM} = 10^{27.6}s$. This is the first analysis developed to place a limit on the gravitino lifetime using IceCube software and simulation files, and the results are comparable to theoretical limits based on the same data set.

DEDICATION

To Nanny Wood and Olivia Rose Pepper

LIST OF ABBREVIATIONS AND SYMBOLS

e	Base of the natural logarithm
$G_{\mu\nu}$	Einstein tensor representing local spacetime curvature
h	Planck constant
i	imaginary number ($\sqrt{-1}$)
k	Boltzmann constant
M_p	Planck mass
R_{sc}	Radius of the Sun's orbit around the center of the Milky Way
$T_{\mu\nu}$	Stress-energy tensor
$\|\nu_\ell\rangle$	Neutrino flavor eigenstate corresponding to lepton flavor ℓ
Λ	Cosmological constant
μ_{90}	Feldman-Cousins 90% upper limit
$\rho_s c$	Local dark matter density
$\rho(x)$	Dark matter density profile evaluated at x
τ_{DM}	Dark matter lifetime
Ω_X	Dark matter mass fraction of the universe

ACKNOWLEDGMENTS

First I would like to thank my advisor Prof. Dawn Williams, who deserves a PhD in patience for seeing this project through to the end, and for dealing with me on a daily basis for nearly eight years. I am also thankful to the Alabama IceCube group for their continued friendship and input over the years: Pat Toale, Donglian Xu, Tomasz Palczewski and Mike Larson.

I would also like to thank my committee members for devoting their time and mental energy to getting myself and my thesis in shape, and for possessing a type of confidence and character that I hope one day to achieve.

Thank you to all my fellow Physics graduate students who helped me stay sane over the years in spite of terrible odds, in particular: Andrea Chaney, Krista McCord, Timmy Brockett, Anna Manning, and Aparajita Sengupta. Special thanks to Sergio Fabi for always outsmarting me, and for being a friend for life.

I owe the deepest gratitude to my amazing family and close-knit circle of friends. This thesis is as much a testament to all of you as it is to me. In particular, my wonderful grandparents, without whom I definitely wouldn't be who I am today. Papa Wood for always quizzing me during dinner, Braves baseball games, and morning notes. Nanny Wood for the Golden Girls and being the most loving person I've ever met. Nanny Pepper for the puzzles, letting me help her cook, and for picking blackberries with me. Papa Pepper for taking care of us in life as well as in death, and for raising my Dad.

To my parents, who've put up with more than any reasonable person should have to, and who always loved me regardless. To my Dad for all the life lessons, practical advice, and leadership over the years. To my Mom for always making me her top priority, for reading to me every night as a child, and for loving me with all of her heart. To my extended parents: Francie Underwood and Larry Hiott. Larry Hiott for loving my mom the way she deserves to be loved. Francie for being a second mom, and for bringing Kat

and the girls (Maeghan Bieri, Sarah Bieri) into our lives. To my nieces for loving me and looking up to me as if I deserved it.

Samantha Katlyn Bailey, for being the love of my life and the best mother to our daughter I could ever ask for. Olivia Rose Pepper, for being the perfect extension of myself and your mother. For giving my life purpose, and for constantly teaching me things I thought I already knew and understood. You are the best thing in my life, and I know you will go on to do great things, and more importantly, be a good person.

To my extended family (Fab4): Ankur Patel, Juan Ruiz, Scott Sutherland, and their families. Thank you guys for being there through the worst times, and being responsible for the best times. Special thanks to Charles Sutherland for his extensive library that contributed to this thesis and for giving myself and Scott a model to live up to.

Finally, special thanks to the people that looked after my parents while I was away writing this damn thing: Jennifer Miller, David Miller, Carolyn Miller, Stan Vonhofe, and anyone else I may be forgetting.

CONTENTS

LIST OF TABLES

LIST OF FIGURES

1 OVERVIEW AND MOTIVATION

1.1 Review of the Standard Model

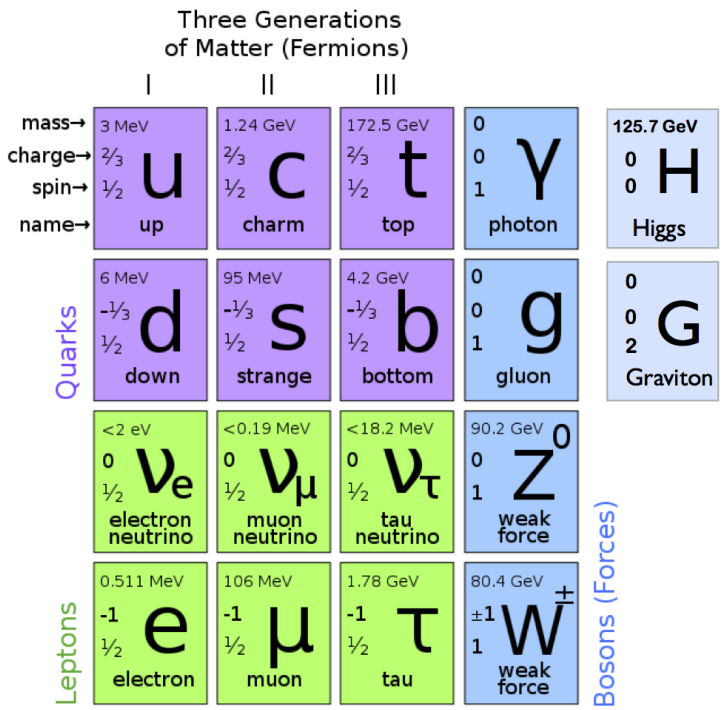

Fig. 1.1.: Particle contents of the Standard Model. Quarks are shown in purple, leptons in green, and bosons in blue. The Higgs boson and the theoretical graviton are shown on the far right. Figure sourced from [1].

The Standard Model (SM) of particle physics (Figure 1.1) describes all of the known particles and their interactions with three of the four fundamental forces (electromagnetic, weak, and strong). Standard model particles can be divided into two classes: fermions and bosons. Fermions are spin-1/2 particles. They obey the Pauli Exclusion Principle which states that no two identical fermions can occupy the same state at the same time, and are described by Fermi-Dirac statistics where the average number in a state i is given by:

$$\bar{n_i} = \frac{1}{e^{(\epsilon_i - \mu)/kT} + 1} \tag{1.1}$$

where ϵ_i is the energy of the i state, μ is the chemical potential, k is the Boltzmann constant, and T is the temperature.

Bosons are particles with integer spins. They are not governed by the Pauli Exclusion Principle, and therefore identical bosons can occupy the same quantum state. These particles are described by Bose-Einstein statistics.

$$\bar{n_i} = \frac{1}{e^{(\epsilon_i - \mu)/kT} - 1} \tag{1.2}$$

Bosons are considered to be the force carriers since the force between two particles can be modeled as the exchange of a virtual boson, which exists only within the time allowed by the uncertainty principle. The bosons in the SM are the photon, $W^{\pm}$, Z^0, the gluon, and the Higgs. The electromagnetic force, for example, acts on electrically charged particles and is mediated by the photon.

Fermion interactions take place through exchange of these bosons. Fermions are subdivided into quarks and leptons. Quarks are distinguished by their ability to interact via the strong nuclear force carried by the gluon. Quarks in the SM are divided into three generations, with the first generation consisting of up and down quarks, the second generation being the charm and strange quarks, and the third generation are the top and bottom quarks. Up, charm, and top quarks have an electromagnetic charge of $+\frac{2}{3}$, while down, strange, and bottom quarks have a charge of $-\frac{1}{3}$. Gluons are responsible for the formation of the quark bound states (hadrons), such as mesons (quark and antiquark) and baryons (three quarks). Protons and neutrons are baryons (up up down, and down down up respectively) and make up the majority of the visible matter in the universe.

Leptons, like quarks, are divided into three generations, with each generation corresponding to a charged lepton and a corresponding neutrino. The charged leptons carry

electric charge of the same magnitude (± 1), with each generation having a heavier mass than the previous generation. The charged leptons in order of generation are the electron, muon, and tau. Leptons do not participate in strong force interactions, but like all fermions, they interact via the weak nuclear force mediated by the $W^{\pm}$ and Z^0 bosons. The $W^{\pm}$ boson also mediates flavor changing quark decays.

Interactions in the standard model can each be described in terms of the internal symmetries of their Lagrangians. Gauge theories describe the continuous group of local transformations under which a Lagrangian is invariant, known as a gauge group. Quantization of the gauge fields results in massless gauge bosons. The fact that the $W^{\pm}$ and Z^0 bosons have a mass can be reconciled with the electroweak gauge theory by the Higgs mechanism. In this framework, all of the gauge bosons were originally massless at high temperatures in the early universe. As the universe expanded and cooled, symmetry was broken, and the W, Z, and Higgs bosons acquired a mass through their interaction with the Higgs field. The existence of the Higgs boson was confirmed by the Large Hadron Collider (LHC) at CERN in 2013 [2, 3].

1.2 Neutrinos

Neutrinos are the least understood particles in the Standard Model. They were first postulated to exist in the 1930s by Wolfgang Pauli after it was noticed that beta decay of atomic nuclei seemed to violate conservation of energy. Furthermore, beta decay produced a continuous spectrum of electron energies, hinting that the process was actually a 3-body decay as opposed to a 2-body decay which would have resulted in monoenergetic electrons. Pauli proposed that the missing energy might be carried away by an unseen third particle. Enrico Fermi later developed a theory of beta decay which included the neutral particles postulated by Pauli, which he dubbed "neutrinos" (little neutral ones) [4].

The existence of the neutrino was later confirmed by Frederick Reines and Clyde Cowan Jr. in 1956 in an experiment conducted at the Savannah River Plant in South

Carolina [5]. The experiment involved using the nuclear reactor on site as an anti-neutrino source. Tanks of water with cadmium chloride added, were placed twelve meters underground and surrounded with tanks of liquid scintillator. The experiment hoped to detect inverse beta decay ($\overline{\nu_e} + p \rightarrow n + e^+$). An incoming antineutrino would interact with the protons in the water and produce a neutron and a positron. The positrons quickly annihilated with electrons into a pair of gamma rays, and the neutrons were captured by the cadmium atoms, which also resulted in the production of a gamma ray. The gamma rays passed through the liquid scintillator and gave off light detected by photomultiplier tubes. The timing between the two gamma rays from the positron decay and the single gamma ray from neutron capture were consistent with the expected results from inverse beta decay. The interaction cross section was measured to be $6.3 \cdot 10^{-44}$ cm^2 in the MeV energy range[5].

In 1962, scientists at Brookhaven National Laboratory published the result of studying pion decay $\pi^{\pm} \rightarrow \mu^{\pm} + (\nu/\overline{\nu})$ [6]. It was noted that the high energy neutrinos created in pion decay resulted in the production of muons, but not electrons. This eventually led to the realization that the neutrinos produced in beta decay (electron neutrinos) were different from the neutrinos produced in their experiment (muon neutrinos). The idea followed that neutrinos had a "flavor" corresponding to a particular lepton. After the discovery of the tau lepton at the Stanford Linear Accelerator in 1974 [7], the existence of a tau neutrino was suspected. This third flavor of neutrino was later confirmed by the DONUT experiment in 2000 [8].

In 1968, the Homestake experiment, which was designed to detect electron neutrinos produced from nuclear reactions in the Sun, measured roughly one-third of the neutrinos predicted by the Standard Model [9]. This led to the so-called "Solar Neutrino Problem." Several years prior, Bruno Pontecorvo published a paper [10] suggesting that if neutrinos had mass, they could oscillate from one flavor to another in a vacuum due to the mass differences between the three flavors of neutrinos. As neutrinos propagate through matter,

the mass eigenstates are altered due to weak interactions with the surrounding medium, and the oscillation lengths change as described by the Mikheyev-Smirnov-Wolfenstein (MSW) effect. This ability to change flavors meant that electron neutrinos produced by fusion reactions in the Sun, could become muon and tau neutrinos. The Sudbury Neutrino Observatory, designed to detect solar neutrinos of all flavors, published results in 2001 confirming that neutrino flavor change, along with the MSW effect, resolved the solar neutrino problem [11].

1.2.1 Neutrino Vacuum Oscillations

Neutrinos are created and interact according to one of three flavor states ($|\nu_e\rangle$, $|\nu_\mu\rangle$, $|\nu_\tau\rangle$). Each flavor eigenstate can be represented as a superposition of the three mass eigenstates ($|\nu_1\rangle$, $|\nu_2\rangle$, $|\nu_3\rangle$) described by the Pontecorvo-Maki-Nakagawa-Sakata (PMNS) matrix U:

$$\begin{pmatrix} |\nu_e\rangle \\ |\nu_\mu\rangle \\ |\nu_\tau\rangle \end{pmatrix} = \begin{pmatrix} U_{e1} & U_{e2} & U_{e3} \\ U_{\mu 1} & U_{\mu 1} & U_{\mu 1} \\ U_{\tau 1} & U_{\tau 2} & U_{\tau 3} \end{pmatrix} \begin{pmatrix} |\nu_1\rangle \\ |\nu_2\rangle \\ |\nu_3\rangle \end{pmatrix} \tag{1.3}$$

where $|U_{\alpha i}|^2$ corresponds to the probability of finding a neutrino of flavor state ν_α in a mass eigenstate of ν_i. In the SM case, where there are three generations of neutrinos, the 3x3 PMNS matrix should be unitary, and can be parameterized with three mixing angles θ_{12}, θ_{13}, θ_{23}, and a phase term δ which relates to violation of CP-symmetry, which states that the laws of physics should be the same if a particle is interchanged with its antiparticle and the chirality of the particle reversed:

$$\begin{aligned} U &= \begin{pmatrix} 1 & 0 & 0 \\ 0 & c_{23} & s_{23} \\ 0 & -s_{23} & c_{23} \end{pmatrix} \begin{pmatrix} c_{13} & 0 & s_{13}e^{-i\delta} \\ 0 & 1 & 0 \\ -s_{13}e^{i\delta} & 0 & c_{13} \end{pmatrix} \begin{pmatrix} c_{12} & s_{12} & 0 \\ -s_{12} & c_{12} & 0 \\ 0 & 0 & 1 \end{pmatrix} \\ &= \begin{pmatrix} c_{12}c_{13} & s_{12}c_{13} & s_{13}e^{-i\delta} \\ -s_{12}c_{23} - c_{12}s_{13}s_{23}e^{i\delta} & c_{12}c_{23} - s_{12}s_{13}s_{23}e^{i\delta} & c_{13}s_{23} \\ s_{12}s_{23} - c_{12}s_{13}c_{23}e^{i\delta} & -c_{12}s_{23} - s_{12}s_{13}c_{23}e^{i\delta} & c_{12}s_{23} \end{pmatrix} \end{aligned} \tag{1.4}$$

where s_{ij} and c_{ij} refer to $sin\theta_{ij}$ and $cos\theta_{ij}$ respectively. The Hamiltonian for relativistic neutrinos is:

$$H = U \begin{pmatrix} E + \frac{m_1^2}{2E} & 0 & 0 \\ 0 & E + \frac{m_2^2}{2E} & 0 \\ 0 & 0 & E + \frac{m_3^2}{2E} \end{pmatrix} U^\dagger \tag{1.5}$$

and the time evolution of the neutrino wave function is given in terms of the initial wave function and the scattering matrix S [12]:

$$\psi(t) = S^{-1}\psi(0)S \tag{1.6}$$

where

$$S = e^{-iH} = U \begin{pmatrix} e^{-i(E+\frac{m_1^2}{2E})} & 0 & 0 \\ 0 & e^{-i(E+\frac{m_2^2}{2E})} & 0 \\ 0 & 0 & e^{-i(E+\frac{m_3^2}{2E})} \end{pmatrix} U^\dagger \tag{1.7}$$

The probability of a neutrino in flavor eigenstate α oscillating to flavor eigenstate β, is given by [12]:

$$\begin{aligned} P_{\alpha\to\beta} &= |S_{\beta\alpha}|^2 \\ &= \sum_j |U_{\beta j} U^*_{\alpha j} e^{-im_j^2/2E}|^2 \end{aligned} \tag{1.8}$$

The mixing angles associated with the PMNS matrix have been measured experimentally and, as of 2016, the current experimental values are [13]:

$$\begin{aligned} \sin^2(2\theta_{12}) &= 0.846 \pm 0.021 \\ \sin^2(2\theta_{23}) &= 0.999^{+0.001}_{-0.018} \\ \sin^2(2\theta_{13}) &= 0.093 \pm 0.008 \end{aligned} \tag{1.9}$$

where the θ_{12} measurement comes from observation of solar neutrinos, θ_{23} from measurements of neutrinos produced in accelerators, and θ_{13} from measurements of nuclear reactor neutrinos.

1.3 Beyond the Standard Model (BSM)

In spite of the many successes of the SM, it contains no explanation of neutrino oscillations or cosmological phenomena such as dark energy and dark matter. And although the standard model accurately describes three of the four fundamental forces, it currently does not contain an explanation for gravity. The electromagnetic, weak, and strong forces are formulated in terms of gauge theories, while gravity is described by general relativity as modifying the geometry of space-time. This effect is described by the Einstein field equations (EFE):

$$G_{\mu\nu} + \Lambda g_{\mu\nu} = \frac{8\pi G}{c^4} T_{\mu\nu} \tag{1.10}$$

$G_{\mu\nu}$ is the Einstein tensor, which represents the local spacetime curvature, Λ is the cosmological constant, $g_{\mu\nu}$ is the metric tensor, G is the gravitational constant, c is the speed of light in a vacuum, and finally $T_{\mu\nu}$ is the symmetric second-rank stress-energy tensor which represents the local energy and momentum content of the spacetime.

Einstein also predicted the existence of gravitational waves that would carry gravitational energy, analogous to electromagnetic waves in electromagnetism. In the same way that the photon is the quantum of electromagnetic waves, attempts have been made [14] to introduce an additional boson to the SM known as the graviton, which would represent the quantization of gravitational waves and mediate the gravitational force. Gravitons are thought to be massless to explain the long range of the gravitational force. In 1965 Weinberg [15] showed that massless spin-2 particles necessarily couple to the second-rank stress-energy tensor in the EFE [15]. Therefore, if gravitons exist they should be massless spin-2 particles.

On September 14, 2015 the Laser Interferometer Gravitational-Wave Observatory (LIGO) made history by being the first to detect the existence of gravitational waves [16]. The signal matches that predicted by general relativity for two black holes merging with a

significance of 5.1σ over background[16]. The source was determined to be two black holes with initial masses of $36^{+5}_{-4}M_\odot$ and $29^{+4}_{-4}M_\odot$ at a redshift of $z = 0.09^{+0.03}_{-0.04}$ [16].

Following the procedure outlined in [17], which relates the frequency of gravitational waves (ν_g) to the Compton wavelength (λ_g) of the graviton:

$$\left(\frac{\nu_g}{c}\right)^2 = 1 - \left(\frac{c}{f\lambda_g}\right)^2 \tag{1.11}$$

where

$$\lambda_g = \frac{h}{m_g c} \tag{1.12}$$

LIGO was able to set an upper bound on the mass of the graviton, $m_g < 1.2 \times 10^{-22}\mathrm{eV/c^2}$.

1.3.1 Dark Matter

There has been a long standing discrepancy between the observed velocities at which luminous matter orbits in galaxies and the velocities predicted by Newtonian gravity. In the 1930s Fritz Zwicky [18], while using the virial theorem to determine the mass of the Coma cluster, calculated a mass much greater than could be accounted for by the visible matter in the cluster. Throughout the 1970s, Vera Rubin [19] measured the rotation speed of galaxies and found that the visible mass of the galaxy alone couldn't provide enough gravitational force to hold the galaxy together. Fritz Zwicky suggested a way of reconciling the theoretical predictions with observation by assuming that the galaxies are actually more massive than they appear. This "extra" matter must be "too dark" to be observed and he therefore coined the phrase "Dark Matter."

The distribution of dark matter should be spherically symmetric about the center of the host galaxy to reproduce the observed velocities. Subsequent observations of low surface brightness (LSB) galaxies and dwarf galaxies indicate a fairly constant dark matter

density in their inner most regions [20], known as a cored dark matter profile. This is in stark contrast to computer simulations which predict a power-law density with a peak (cusp) at the center of the galaxy [21]. The halos produced in computer simulations have density profiles best described by the Navarro-Frenk-White (NFW) model[22],

$$\rho_{NFW} = \rho_H \frac{1}{x(1+x)^2} \tag{1.13}$$

While observations are better fit with the Burkert density profile[22],

$$\rho_{Bur} = \rho_H \frac{1}{(1+x)(1+x^2)} \tag{1.14}$$

Where ρ_H is the scale density, and $x = r/R_H$ where r is the distance from the center of the galaxy and R_H is the scale radius. A side-by-side comparison in arbitrary units is shown in Figure 1.2.

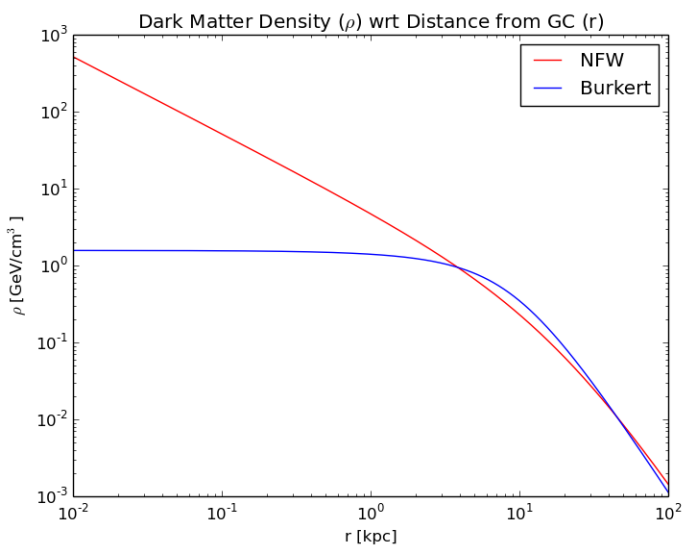

Fig. 1.2.: The Burkert profile (blue) describes a dark matter halo profile with a constant inner density, which is a better fit to observations than the NFW profile (red), which best describes computer simulated halos with an inner density strongly peaked at the center.

One possible explanation comes in the form of "dark" astrophysical objects. Mas-

sive Compact Halo Objects (MACHOs) such as black holes, neutron stars, brown dwarfs, Jupiter-like planets, and other baryonic matter would be hard to detect and were thought to possibly account for the unseen matter in galaxies. However, Big Bang Nucleosynthesis (BBN) is highly sensitive to the baryon density of the early universe [23]. If dark matter were composed mostly of baryonic matter, it would conflict with the BBN prediction of the abundances of lighter elements [24, 25]. This strongly constrains the amount of baryonic matter that could contribute to dark matter. Furthermore, measurements of the Cosmic Microwave Background (CMB) also suggest that the contribution of baryonic matter to the total dark matter density must be small [13].

Alternatively, MOdified Newtonian Dynamics (MOND) suggests that, rather than galaxies having a large dark population, galaxy rotation curves could be explained by modifying the gravitational force such that it is proportional to $1/r$ at large scales instead of $1/r^2$. This negates the need for dark matter and suggests that gravity isn't well understood at large scales. Although interesting, these theories have several issues explaining objects such as the Bullet Cluster, which is the result of two galaxy clusters colliding. Gravitational lensing shows the majority of the resulting cluster's mass lies outside of the luminous matter. MOND predicts the gravitational lensing should follow the baryons and not the dark matter. Additionally, due to the fact that in the modified case, $F_g \propto \frac{1}{r}$, the gravitational potential V_g is proportional to $ln(r)$. Therefore the potential would never become zero, making escape velocities impossible unless the external field effect due to other galaxies is considered [26].

From a particle physics perspective, the only particle from the Standard Model that satisfies the conditions for a dark matter candidate is the neutrino, which is massive, stable, electrically neutral, and weakly interacting. However, due to the neutrino's small mass, it is extremely relativistic. Simulations of the Large Scale Structure (LSS) [27] show that if dark matter is too relativistic (hot), the effective cross section to capture these particles becomes too low, the particles pass by each other, and structure formation

becomes washed out. This, along with the BBN and CMB constraints, motivated searches for cold/warm dark matter beyond the Standard Model (BSM). Many BSM theories exist to explain other natural phenomenon and also happen to contain a particle that satisfies the conditions of a dark matter candidate. The most well motivated candidates include axions, sterile neutrinos, and Weakly Interacting Massive Particles (WIMPs) [13].

Axions are theoretical neutral, massive bosons postulated to resolve the strong CP problem in quantum chromodynamics (QCD). The QCD Lagrangian could contain terms that violate CP-symmetry. At the present, no experimental results have ever detected CP-violation in QCD. Pecci-Quinn theory proposed to explain this by having a CP violating term in the QCD Lagrangian parameterized by a field θ. The particles that would result from this field, are known as axions [28].

All experimentally observed neutrinos have a spin opposite to their momentum, known as "left-handed" neutrinos. Experimental verification of the neutrino mass [29] implies that there could be a right-handed neutrino. These right-handed neutrinos can have a wide range of masses, but when they are light they are called "sterile neutrinos" [30]. Sterile neutrinos do not participate in electroweak interactions, which allows them to be a potential dark matter candidate. In the keV mass range, these neutrinos could resolve the cusp/core discrepancy between halo simulations and observations [31]. Sterile neutrinos could potentially decay via $\nu_s \rightarrow \nu + \gamma$ [32], and the resulting monoenergetic photons with an energy equal to $\frac{m_{DM}}{2}$ could, depending on the mass, be observed by X-ray satellites.

WIMPs are particles with a mass in the GeV - TeV range [33], which were initially in thermal equilibrium with the early universe. During this phase, the amount of WIMPs being produced was equal to the amount lost via self-annihilation. As the universe expanded and cooled, the average energy of particle interactions fell below the mass of the WIMP and therefore they could no longer be produced. This process whereby the WIMP falls out of equilibrium with the early universe is known as "freeze-out" and would result

in a relic abundance of WIMPs. In order for a thermal relic to produce the correct relic abundance in agreement with observations, the interaction cross section must be near the weak scale ($\sigma \approx 0.1$pb). This surprising result is known as the "WIMP Miracle" and is one of the primary motivations of WIMP searches [34]. Using an approximation of the Boltzmann equation, the dark matter mass fraction (Ω_X) is,

$$\Omega_X h^2 \simeq \frac{s_0}{\rho_c/h^2}\left(\frac{45}{\pi^2 g_*}\right)^{1/2}\frac{1}{x_f M_p}\frac{1}{<\sigma_{ann} v>} \tag{1.15}$$

where h is the dimensionless hubble parameter, s_0 is the present day entropy density of the Universe, ρ_c is the density required for the universe to stop expanding without collapsing in on itself (estimated to be $1.05 \cdot 10^{-5}$ h^2 GeV cm^{-3} [13]), g_* the number of degrees of freedom at freeze-out, M_p is the Planck mass, x_f is the ratio of freeze-out temperature to the mass of the particle ($T_{fr}/m_X \sim 1/25$), and σ_{ann} is the annihilation cross section. Using known values from [13] and setting $\Omega_X h^2$ to the measured value of $\simeq 0.12$, the annihilation cross section (σ_{ann}) is found to be on the order of the weak scale $\sim 10^{-36}$cm^2($= 1$ pb).

Many WIMP searches focus on dark matter candidates from Supersymmetric (SUSY) theories. Conveniently, SUSY predicts unification of the force interactions in the standard model at high energies. This is achieved by adding extra terms to the interaction Lagrangian that contain, for every SM particle, a superpartner with an additional $+\frac{1}{2}$ spin. Every SM fermion has a bosonic superpartner, and every SM boson has a fermionic superpartner (Table 1.1). In SUSY DM theories the lightest particle should be stable and neutral. These lightest stable particles (LSP) are generally in the form of neutralinos (mixture of gauge boson superpartners) or gravitinos (superpartner of graviton). The search for gravitinos is the primary focus of this analysis.

SM particle	Superpartner
quarks	squarks
leptons	sleptons
neutrinos	sneutrinos
photon	photino
W	wino
Z	zino
gluon	gluino
higgs	higgsino
graviton	gravitino

Table 1.1.: SM Particles and their corresponding Superpartners.

1.3.2 Gravitinos

With the exception of gravity, the interactions of all of the forces can be modeled using force carrying bosons. For electromagnetism, this is accomplished with the photon, for the weak force the charged $W^{\pm}$ bosons and neutral Z^0 boson, and the strong force is carried by the gluons. Following this logic, it is natural to assume the existence of an additional boson called the graviton that would carry the force of gravity. Supersymmetric theories that include the graviton are known as Supergravity (SUGRA). If a particle exists in the Standard Model, according to SUSY it must have a superpartner. The superpartner of the spin-2 graviton is the gravitino, a spin-3/2 fermion.

In general, SUSY models require conservation of a quantum number known as R-parity described by:

$$R_p = (-1)^{3(B-L)+2S} \tag{1.16}$$

where B is baryon number, L is lepton number, and S is spin. Conservation of R-parity serves to kinematically disallow processes that lead to rapid decay of the proton [35]. This results in all SUSY particles having $R_p = -1$ (odd parity), while all SM particles have $R_p = +1$ (even parity). In models where R-parity is conserved, then, the LSP is stable as there are no lighter SUSY particles for the LSP to decay into, and decay to SM particles

is forbidden since it would not conserve R_p. However, in SUSY models where the gravitino is the LSP and R-parity is conserved, the next-to-lightest supersymmetric particle (NLSP) can interfere with predictions of BBN [36]. Since the NLSP can only decay to the gravitino and SM particles, it generally survives until after nuclei have started to form in the early universe. The products of the NLSP decay then interfere with the primordial elements and throw off the BBN predictions which agree with observation.

If, however, R-parity is not completely conserved, the NLSP can safely decay to SM particles before the ligher elements have started to form. Even though the gravitino is no longer stable in this scenario, it can still have a lifetime orders of magnitude longer than the age of the universe due to the suppressed gravitino interactions and small R-parity breaking, and thus be a suitable candidate for cold dark matter [37]. Due the fact that gravitino interactions are Planck scale suppressed, they would immediately decouple from the thermal plasma of the early universe regardless of their mass [37]. This leads to theories where the gravitino can have a mass on the order of a PeV, and be a candidate for very heavy dark matter (VHDM).

It has been speculated [38, 39, 40, 41, 42] that the recent observed flux of extraterrestrial neutrinos with energies ranging from 30 TeV to 2 PeV [43, 44] could originate from the decay of VHDM. This type of DM could decay with lifetimes much longer than the age of the Universe, producing neutrinos in the same energy range as the high energy events observed by IceCube [38, 39, 40, 41, 42]. In the case where the gravitino is VHDM, neutrinos from decaying gravitino dark matter should arrive with a unique energy spectrum and a directional distribution proportional to the dark matter density of the galaxy.

1.3.2.1 Gravitino Two-body Decays to Neutrinos

As previously discussed, in theoretical models that predict a gravitino LSP with R-parity violating terms, the gravitino can decay into standard model particles. In most models, the two-body decay modes are the dominant channels by which a gravitino can

decay [36]. The observed flux of neutrinos from gravitino DM decay depends on the distribution of DM in the Milky Way, its lifetime, and decay spectrum. In the following we will focus on the decay of gravitino DM as outlined in [36] and consider two-body decays into $\gamma\nu$, $Z\nu$, $h\nu$, and $W^+\tau^-$.

Due to the fact that gravitinos are spin-3/2 particles, they are kinematically allowed to decay to a spin-1 boson and a fermion. The majority of these two-body decay modes result in very distinct neutrino energy spectra. For a quantitative discussion of the resulting neutrino energy spectra, refer to Chapter 3. Branching ratios for gravitino decay modes are highly model dependent. Therefore, in an effort to remove model dependencies as much as possible, this analysis considers each decay product individually and sets limits for 100% branching into each.

One possible decay mode of the gravitino results in a photon and neutrino in the final state. It described by the following Feynman diagram [36]:

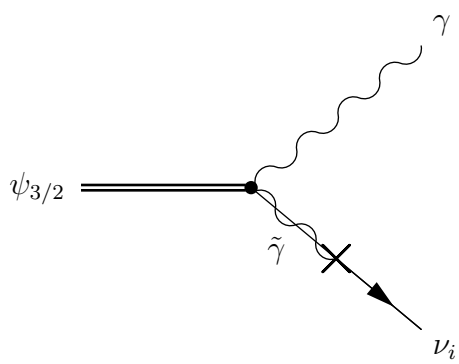

In this scenario, the gravitino couples to the photon and the photino ($\tilde{\gamma}$) and a neutrino is produced via the R-parity violating photino-neutrino mixing. The resulting neutrinos are monoenergetic and would result in a line in the neutrino energy spectrum at half the gravitino mass.

For a gravitino mass of 2 PeV, which is the mass considered in this analysis, decay to $W^{\pm}$ and Z^0 bosons are allowed. For production of each boson, two tree-level diagrams contribute: one involving the mixing between the superpartner (Wino ($\tilde{W}$) and Zino ($\tilde{Z}$) respectively) and the neutrino, and one involving the Higgs vacuum expectation value

(VEV). Decay to a W boson is described by the following Feynman diagrams [36]:

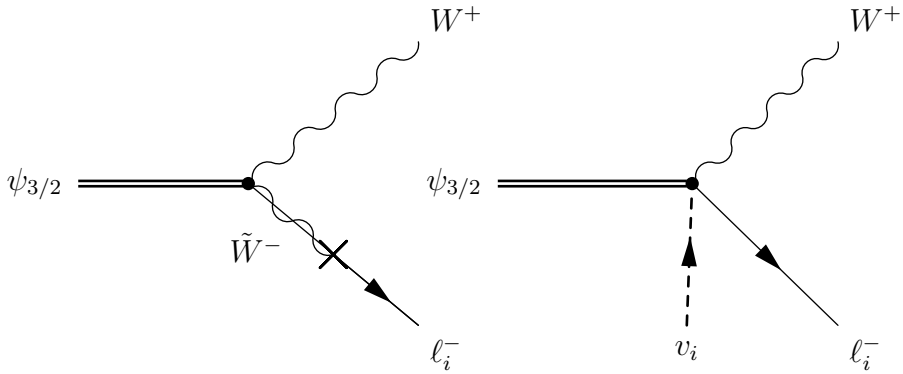

The resulting W boson then continues to decay producing a continuous spectrum of neutrinos. In the case where the lepton is a muon or tau, additional neutrinos can be produced as they decay.

Because the Z^0 boson is neutral, like the photon, the other final state particle must also be neutral, such as a neutrino, which is monoenergetic. Unlike the photon, however, the Z boson can continue to decay producing a continuous spectrum of neutrinos. The corresponding Feynman diagrams are [36]:

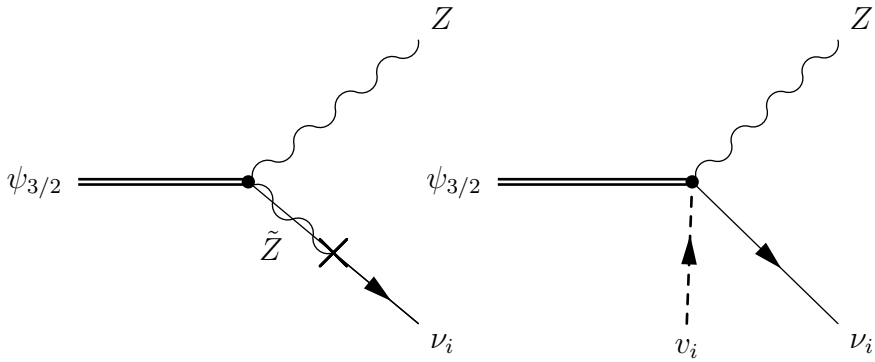

Decay to the lightest Higgs boson occurs via neutral Higgs-sneutrino mixing and neutral higgsino-neutrino mixing as shown in the following Feynman diagrams:

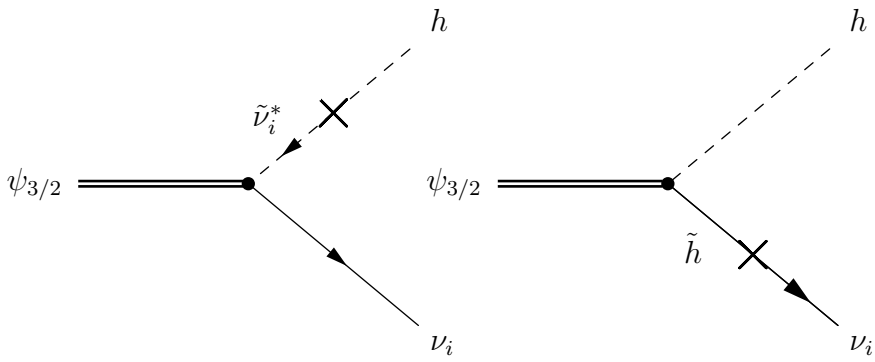

Neutrinos resulting from decay into a scalar Higgs boson have a similar characteristics with the Z boson decay mode in that there is monoenergetic neutrino production at half the gravitino mass, as well as a continuous spectrum of neutrinos produced by further decay of the Higgs.

2 DETECTOR DESCRIPTION

2.1 IceCube Neutrino Observatory

The IceCube Neutrino Observatory (Figure 2.1) is a neutrino detector located at the geographic South Pole. Construction began in 2005 and was completed in December of 2010. The detector consists of 86 cables, known as "strings", deployed in the Antarctic ice with a horizontal spacing of 125 m. Each string is instrumented with 60 Digital Optical Modules (DOMs) (Figure 2.2), which consist of a photomultiplier tube (PMT) in a glass pressure vessel, along with a digitizing motherboard. The DOMs are deployed at 17 m intervals along the strings from about 1.5 km to 2.5 km deep in the ice, instrumenting a cubic kilometer of ice.

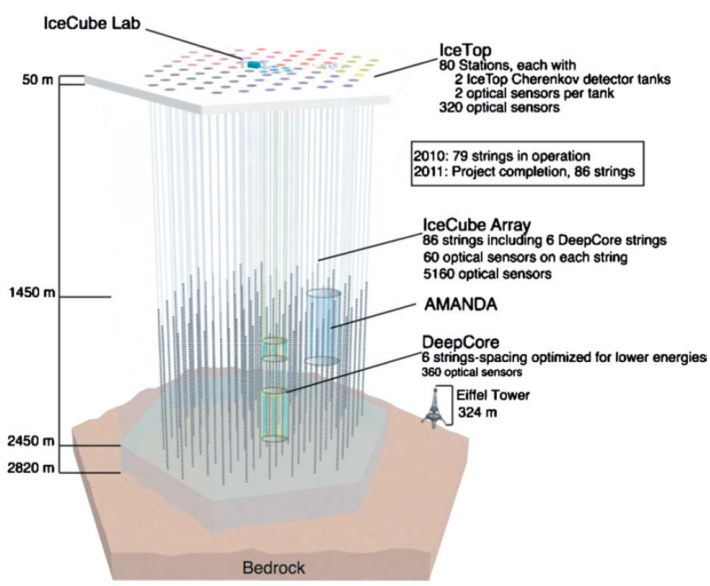

Fig. 2.1.: Depiction of the IceCube Neutrino Observatory, including string positions and instrumentation depth. DeepCore is the densely instrumented green cylinder, and AMANDA is the decommissioned predecessor of IceCube.

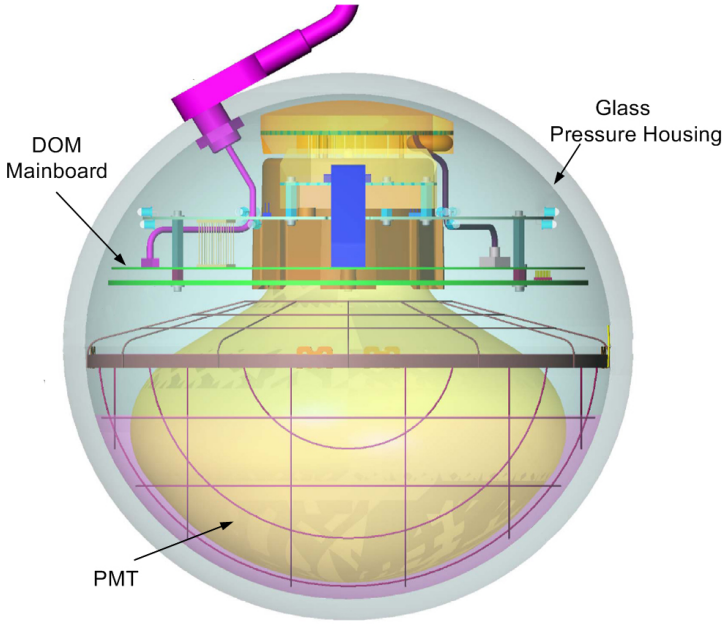

Fig. 2.2.: Diagram of an IceCube DOM and its constituent parts.

The IceTop array consists of tanks filled with clear ice for studying cosmic rays. There are two tanks, separated by 10 m, at the surface above 81 of the IceCube strings, instrumenting a total area of 1 km^2 [45].

DeepCore consists of 15 strings closely spaced in the center of IceCube. Eight of the strings are instrumented with 60 high quantum efficiency (HQE) PMTs. From 2100m to 2450m, 50 DOMs have a vertical spacing of 7 m. The region from 2000m to 2100m is not instrumented due to the high absorption from particulate matter in the ice at those depths, known as the "dust layer". Above the dust layer, 10 DOMs with a vertical spacing of 10m act as a veto for down going muons. The HQE DOMs are about 35% more efficient than the DOMs on standard IceCube strings. DeepCore is located near the bottom of the detector, in extremely clear ice. This closer spacing and greater sensitivity to light, allows for better resolution of low energy events down to around 10 GeV, compared to 50-100 GeV for standard IceCube strings. For these reasons, DeepCore increases IceCube's sensitivity to low energy WIMP annihilation, neutrino oscillation, and supernovae neutrinos [46].

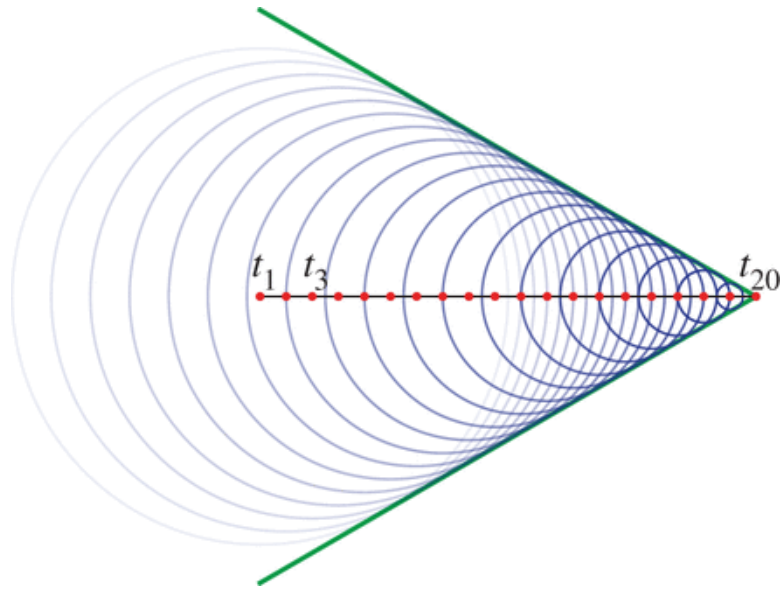

Fig. 2.3.: Diagram depicting Cherenkov radiation as spheres of light traveling outward. The particle is traveling faster than the light being produced can propagate, thus creating a cone shape. Figure was taken from [47].

When a charged particle travels through a dielectric medium (such as ice) faster than the speed at which light propagates in that medium, it produces a blue cone of light known as Cherenkov radiation (Figure 2.3). The opening angle of the cone is related to the velocity of the particle (v_p) and the refractive index (n) of the medium by

$$\cos(\theta) = \frac{1}{n\beta} \tag{2.1}$$

where $\beta = \frac{v_p}{c}$.

Charged particles in the ice also produce light via muon bremsstrahlung, photonuclear interactions, and pair production. The IceCube DOMs detect the light emitted by particles undergoing the aforementioned processes, and send timing and charge information to the surface. The timing and amount of charge deposited in the DOMs is used to reconstruct the direction from which the particle came, the energy of the particle, the position in the detector where the interaction took place, as well as the time the interaction occurred.

2.2 DOM Description

IceCube consists of over 5000 DOMs and digitizing electronics, each fitted with a 10" diameter Hamamatsu R7081-02 photomultiplier tube (PMT)[48]. PMTs detect light from neutrino interactions in the ice. This signal is then digitized and timestamped by the DOM mainboard and sent to the surface, where the IceCube Laboratory (ICL) collects the data [49].

When photons hit a PMT photocathode they may eject an electron due to the photoelectric effect. The electron is then accelerated towards a dynode. When the electron hits the dynode, it causes the release of multiple secondary electrons which then interact with another dynode, thereby increasing the total number of electrons associated with the incident photon. By repeating this process multiple times, detection of single photons is possible.

The collection efficiency of the PMT depends on many things, such as the temperature and quantum efficiency of the PMT, as well as the angle and frequency of the incident light. PMT efficiency at a particular part of the photocathode may vary up to 40% between PMTs, but when integrated over the entire area of the photocathode, the spread from PMT to PMT is closer to 10% [48]. The efficiency of IceCube PMTs were measured by shining a laser through nitrogen gas onto the PMT at various angles and temperatures ranging from +25° C to -45° C. The PMTs were shown to have an optical efficiency of around 22% [46]. In-situ measurements of the HQE DOM optical efficiencies showed a 35% improvement over standard IceCube DOMs [46].

The analog PMT waveform is digitized by the Analog Transient Waveform Digitizers (ATWDs) on the DOM mainboard, which have a 422 ns data acquisition window [49]. The waveform is divided into 128 samples by the first ATWD channel which amplifies the signal by a factor of 16. If any sample exceeds 768 counts, the signal is then digitized by a second ATWD channel at x2 gain. Likewise, if the second ATWD channel overflows, the third

ATWD channel then digitizes with a gain of x0.25. The digitization takes 29 μs from capture to digitization [48]. To decrease downtime during the digitization process, each DOM is equipped with two ATWD chips to allow one to capture signal while the other is digitizing.

Because some signals can last longer than the ATWD digitization window, each DOM has a fast analog to digital converter (FADC) with a time window of 6.4 μs and a digitization time of 180 ns [50].

Each DOM also contains a "flasher" board of 12 LEDs that can be activated in various patterns to calibrate other DOMs, study light propagation in the ice, or simulate physics events.

In order to extract accurate timing and charge information from the digital waveform, the DOMs must be accurately calibrated. These calibrations are all handled by on-board software known as DOM-Cal which is discussed in detail in [51]. Timing calibration involves sending signals from the surface to the DOM, and having the DOM send identical reciprocal signals back to the surface and measuring the waveform spread. The differences in the round trip time between calibrations gives a basic measurement of the time calibration precision, which is less than 2ns RMS [51]. Charge calibration is performed by flashing the on-board LED at a low intensity such that there is $<<$ 1 photoelectron (p. e.) in the PMT, and fitting the charge distribution to find the single photoelectron peak.

2.3 Triggering

A DOM begins recording data when a PMT signal exceeds the discriminator threshold of 0.25 p.e., referred to as a "hit". The rate at which DOMs are hit due to dark noise and radioactive decays in the glass is around 300 Hz per DOM [52]. Due to the limited bandwidth of the cables, a decision must be made quickly whether or not to send the event to the surface.

When a DOM is hit, it sends a pulse to neighboring DOMs on the same string.

This local coincidence (LC) pulse allows DOMs to communicate, and only send their data to the surface if their neighbors were also hit within a given time window. This increases the likelihood that the hit is due to a physics event rather than DOM noise.

A Soft Local Coincidence (SLC) hit occurs when a DOM and one of its nearest neighbors are hit within a 800 ns time window. Hard Local Coincidence (HLC) hits occur when a DOM and two of its nearest or next-to-nearest neighbors register a hit within a ± 1 microsecond time window [53].

At the surface, certain conditions (triggers) must be met in order for an event to be considered interesting enough for further processing. Triggers are basic conditions designed to keep interesting events at the cost of accepting background events. Some examples are the Simple Multiplicity Triggers (SMT) which require a certain number of DOMs on a string to register a hit. IceCube triggers when eight or more HLC hits occur within a 5 microsecond time window, known as a Simple Multiplicity Trigger (SMT8). When such an event occurs, data from ± 10 microseconds before and after the event is read out, reducing the event rate to around 3 kHz [46]. Events that pass basic trigger requirements then go on to have filters applied, which reduce the amount of background events.

2.4 Filtering

All triggered data is stored on tapes or disk at the South Pole which are transferred North during the Austral summer. In order to reduce the amount of data sent North via satellite, triggered data is processed by filtering software which runs basic reconstruction algorithms, basic likelihood fitting algorithms, and select for certain event topologies such as extremely high energy events, cascades, and upgoing muons [53]. This analysis uses no specific filter.

2.5 Particle Interactions in the Detector

When an incoming neutrino enters the detector, it can interact with the protons and neutrons in the ice via exchange of a Z^0 (neutral current (NC) interaction) or a $W^{\pm}$ (charged current (CC) interaction) boson (Fig. 2.4).

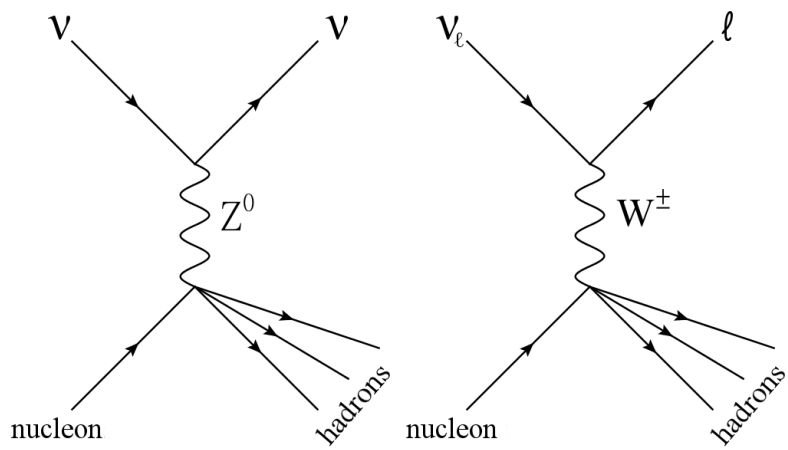

(a) Neutral Current Interaction (b) Charged Current Interaction

Fig. 2.4.: These images depict the neutral current and charged current interactions. In both cases, there is a hadronic shower due to hadronization of the quarks. In the charged current interaction, there is also a charged lepton produced that will interact in the ice.

2.5.1 Neutral Current Interaction

During a neutral current interaction, the incoming neutrino loses energy via Z^0 exchange with a quark inside a nucleon in the ice. This process, known as Deep Inelastic Scattering (DIS) and is the dominant neutrino interaction cross section at and above neutrino energies on the order of a TeV. DIS leads to hadronization of the nucleon, resulting in the production of mesons (mostly pions).

The pions then decay further. The neutral pion, π^0, decays into two gamma rays with 99% probability, and the charged pion, $\pi^{\pm}$, decays into $\mu^{\pm}$ with greater than 99% probability. The muons lose their energy to ionization, whereas the gamma rays can undergo pair production or continue to DIS with other baryons in the ice, producing more

unstable mesons which then further decay.

The light resulting from the particles and daughter particles involved in the hadronization is known as a hadronic shower, and produces a nearly spherical (due to scattering) distribution of light in IceCube, called a "cascade" (Figure 2.5 right-side).

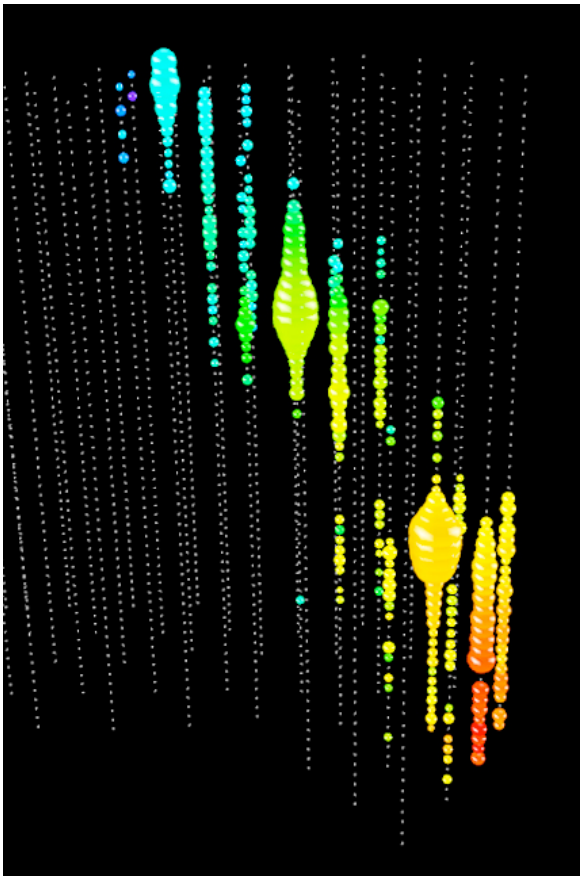

(a) Simulated track event

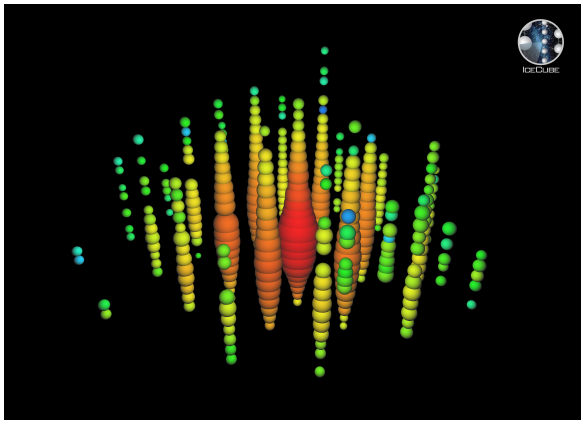

(b) Observed 1.14 PeV cascade event known as "Ernie"

Fig. 2.5.: Examples of track (left) and cascade (right) event topologies in IceCube. Figures taken from [54] and [55] respectively. The size of the spheres represent the amount of light collected by each DOM, and the colors are associated with timing, with red to blue representing early to late hit DOMs.

2.5.2 Charged Current Interaction

Charged current interactions occur when the incoming neutrino scatters via a $W^{\pm}$ boson and is converted to its corresponding charged lepton. At energies relevant to Ice-

Cube, this scattering occurs with a nucleon in the ice, and the interaction with the quarks results in hadronization similarly to the neutral current interaction.

In the case of a ν_e charged current interaction, the electron produced will quickly lose energy to bremsstrahlung radiation (above $\sim$10 MeV), and then ionization losses (below $\sim$10 MeV). The photons produced by the electron scattering can undergo pair production, producing electrons and positrons. These particles will also lose their energy quickly to Bremsstrahlung. This process is known as an electromagnetic cascade, which produces a cascade in the detector like the hadronic shower. The typical cascade length is 10m [56], which is less than the interstring spacing (17 m) of IceCube. IceCube cannot distinguish between hadronic and EM cascades.

In the case of a ν_μ charged-current interaction, the resulting muon will lose much less energy via bremsstrahlung than the electron due to the inverse mass dependence of bremsstrahlung. The power radiated by bremsstrahlung is proportional to between $1/m^4$ and $1/m^6$. This means that the muon can travel large distances while emitting bremsstrahlung and Cherenkov radiation. This results in a "track" of light through the detector (Figure 2.5 left-side).

Taus lose even less energy than muons to bremsstrahlung, but are very short lived ($\sim 10^{-13}$s). Taus decay quickly to muons or electrons with roughly equal ($\sim$17%) probabilities. The daughter muons (electrons) will interact and create tracks (electromagnetic cascades). The other possibility is for the tau to decay into hadrons, which would result in hadronic showers. Tau topologies vary depending on the energy and the position in the detector where the interaction occurs. Most tau interactions will appear as cascades.

2.5.3 Glashow Resonance

In 1960, Sheldon Glashow described a resonance for forming the W-boson in collisions between electrons and electron anti-neutrinos [57]. The relevant process is,

$$e^- + \bar{\nu}_e \rightarrow W^- \tag{2.2}$$

The neutrino interaction cross-section for this process increases drastically at 6.3 PeV, and thus the effective area of the detector to electron neutrinos at this energy (Figure 2.6).

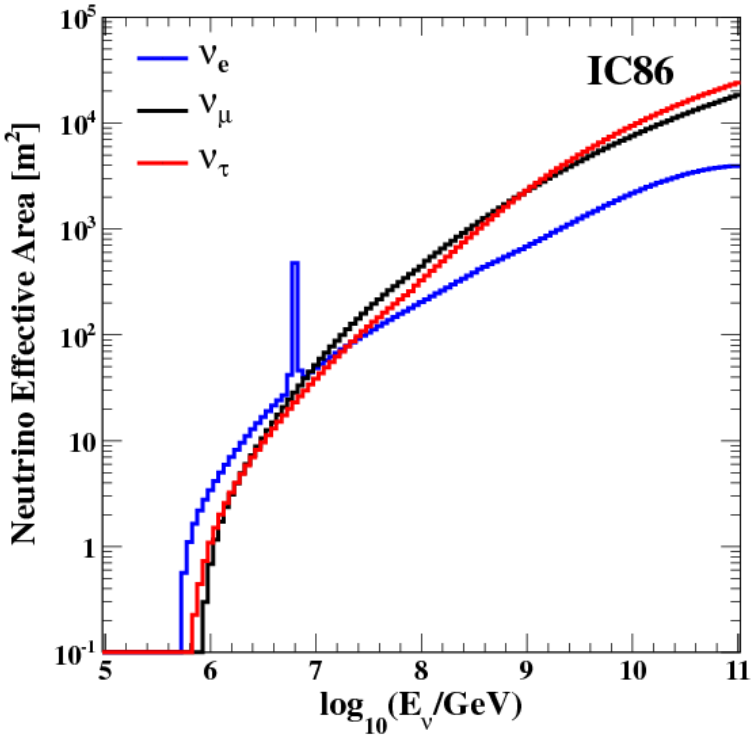

Fig. 2.6.: Effective area of IceCube as a function of energy for all flavors of neutrinos. The sharp peak in the electron neutrino effective area at 6.3 PeV corresponds to the Glashow resonance. Figure was taken from [58].

2.6 Atmospheric Neutrinos

Cosmic rays interact in the upper atmosphere (Figure 2.7) leading to the production of pions, kaons, and a small number of heavier mesons. Pion and kaon decay lead to what is known as the "conventional" atmospheric neutrino flux. Neutral pions decay quickly ($8 \cdot 10^{-17}$ s [13]) to two photons, leading to an electromagnetic shower. Charged pions decay to $\mu\nu_\mu$ or at higher energies, interact with nucleons in the atmosphere producing more lower energy pions. Kaons are produced in air showers at a tenth of the rate of pions [59], but decay faster to neutrinos ($\mu\nu_\mu$ and $e\nu_e$). The faster decay leads to higher energy neutrinos, and can even dominate the atmospheric neutrino spectrum above 100 GeV [60] in spite of their limited production relative to pions. Pion and kaon decay dominates the atmospheric neutrino spectrum up to 500 TeV, and follows a power-law one power steeper than the primary cosmic ray spectrum ($\frac{dN}{dE} \propto E_\nu^{-3.7}$) [61]. The conventional flux is modeled in this analysis with [62] along with corrections above the knee given in [63].

Heavier hadrons containing charm quarks can also be produced by cosmic rays, but are strongly suppressed. The decay of these heavier, shorter-lived mesons, leads to a harder spectrum of neutrinos, known as the "prompt" atmospheric neutrino flux, which is expected to dominate at energies above 100 TeV [65]. The prompt flux has never been directly observed, but upper limits have been set by [65]. Theoretical predictions of the prompt flux are given in [66]. For this analysis, the prompt flux was considered to be equal to the upper bound so as to yield the most conservative result. The atmospheric neutrino flux represents an irreducible background in this analysis, but the neutrino spectrum is well measured at low energies [67] and is expected to follow the primary cosmic ray spectrum in the PeV range and should be distinguishable from a potential dark matter signal.

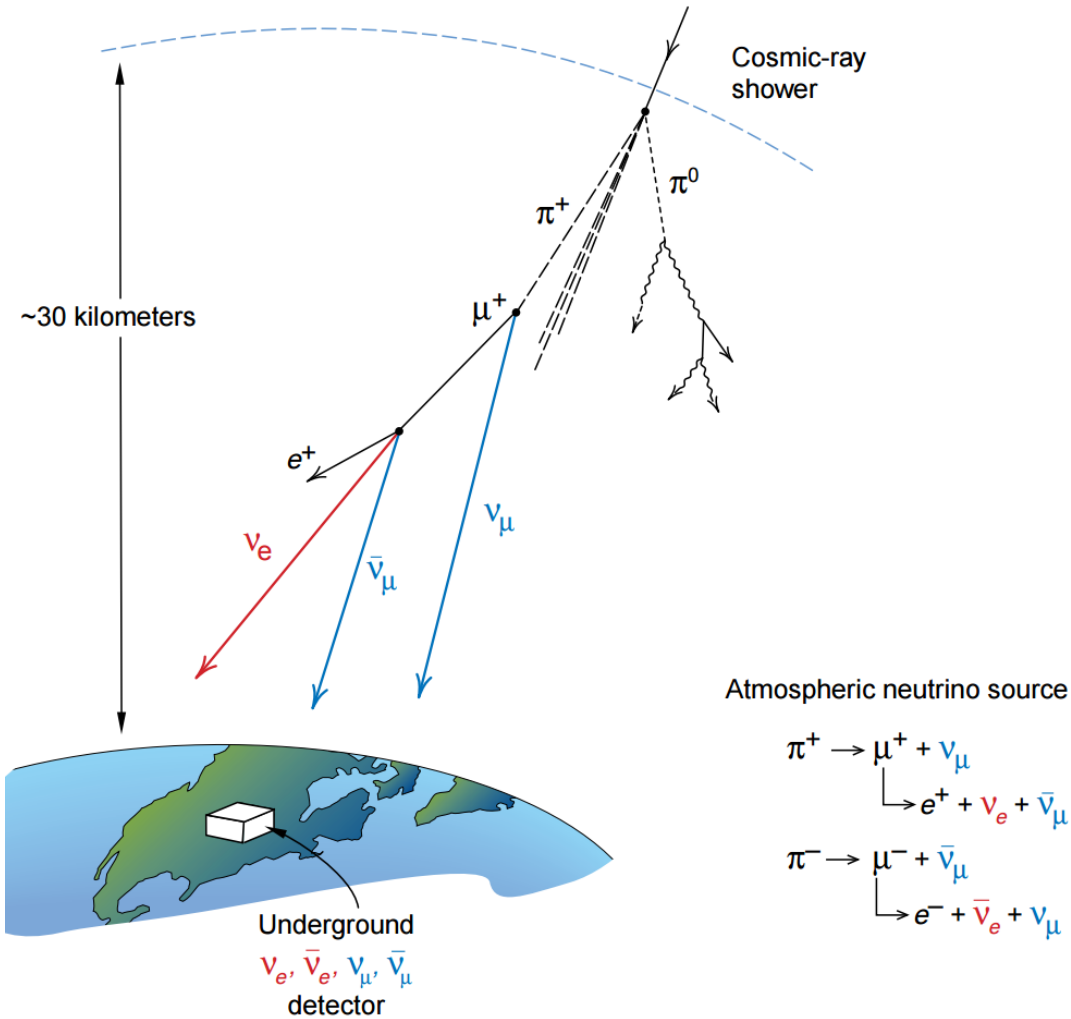

Fig. 2.7.: Depiction of a cosmic ray interacting in the upper atmosphere leading to production of neutrinos. Figure was taken from [64].

2.7 Modeling the Ice

Understanding and modeling the optical scattering and absorption in the ice is necessary for reconstructing neutrino events in the detector and photon propagation in simulation. The ice model must also consider the differences between bulk ice and hole ice. Bulk ice refers to the volume of ice left undrilled during construction, which contains volcanic ash and dust impurities. The hole ice refers to the ice melted during the drilling

process that refroze around the strings. Hole ice contains more bubbles than the bulk ice. Since the bubbles are larger than the wavelength of the incoming light, the scattering is best described by Mie scattering, where an electromagnetic wave scatters off a homogeneous sphere. The ice model used in this analysis is SPICE-Mie [68] which models these effects and also accounts for tilt in the dust layer. The most recent ice model, SPICE-Lea [69], is based on SPICE-Mie but adds an anisotropic scattering component to create a better fit to flasher data. SPICE-Lea was not widely implemented until after 2011, and therefore was not used in this analysis.

2.8 Detection of Astrophysical Neutrinos

Astrophysical neutrinos are thought to be produced by astrophysical accelerators such as supernovae, pulsars, molecular clouds, gamma-ray bursts (GRBs) and active galactic nuclei (AGN). These environments contain strong magnetic fields ideal for accelerating charged particles due to Fermi acceleration, where a charged particle is repeatedly accelerated by inhomogenous magnetic fields around a shock front. Ultra high energy neutrinos (> 100 TeV) can only be produced by the most extreme astrophysical environments such as AGN and GRB, which are thought to be responsible for the highest energy cosmic rays. If these cosmic rays decay to neutrinos before losing energy to the surrounding environment, the neutrino energy spectrum should follow an E^{-2} spectrum. Although this spectrum can change depending on the surrounding environment, it is generally thought to be between $\mathrm{E}^{-1.5}$ and $\mathrm{E}^{-2.5}$ [70].

In 2013, IceCube published a measurement of the astrophysical neutrino flux at high energies (30 TeV - 2 PeV) over the course of two years[43]. This resulted in the detection of 28 high energy neutrino events. The energy and declination distribution of the events is show in Figure 2.8. A purely atmospheric hypothesis was rejected at a level of 4σ significance (later 5.7σ in 2014 [44]). A power law spectrum was fit to the data and is slightly softer ($E^{-2.3}$) than the E^{-2} spectrum expected from astrophysical accelerators

such as GRBs and AGN. Although the spectrum does appear to deviate from a power law around 0.5 PeV - 1 PeV (Figure 2.8), the low statistics mean it could be merely due to statistical fluctuation.

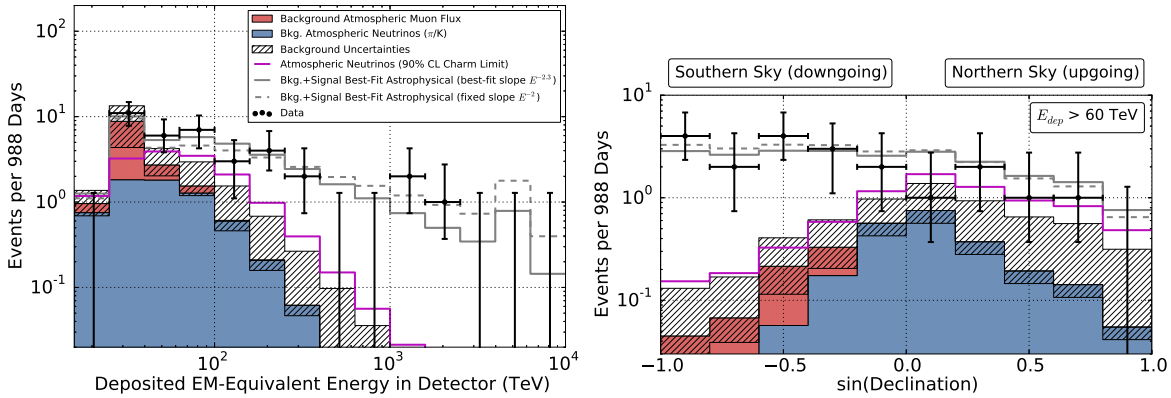

(a) Energy distribution (b) Declination distribution

Fig. 2.8.: Energy and declination distributions for the high energy starting events in IceCube. There was no significant clustering in arrival direction. There appears to be a "gap" between about 0.5 PeV and 1 PeV, although this could be due to statistical fluctuations. Figures taken from [44].

This analysis applies the same event selection as in [43, 44]. This event selection is known as the High Energy Starting Event (HESE) selection and is described in detail in Chapter 5. HESE was primarily a cascade analysis, and was followed up by a high energy muon neutrino (track) search [71]. The results of the track analysis found that the highest energy events were inconsistent with a terrestrial origin at 3.7σ, and a best fit astrophysical spectral index of $E^{-2.2}$, which is in good agreement with the HESE analysis.

3 SIMULATION

Simulated events in IceCube are created by software packages designed to handle particle generation, particle propagation, photon propagation, and detector response. All simulated neutrino events used in this analysis were created by this chain of software packages. This includes neutrinos produced in the atmosphere, by astrophysical sources, and of dark matter origin. The cosmic ray muon background for most IceCube analyses are simulated using a package known as CORSIKA [72]. However, due to the simplicity of the HESE selection the background can be estimated from data by tagging previously vetoed events, and allowing them to pass through to the next layer of strings. From this, the probability of a muon passing the veto can be derived as a function of the number of veto layers and the energy of the incoming muon. At the energies considered in this analysis, there are around 3 ± 1.7 muon background events per year [44].

3.1 Neutrino Event Simulation

Neutrinos are first generated by *Neutrino Generator* (NuGen) [73], which produces neutrinos of any flavor corresponding to a specified flux, with energies ranging from 10 GeV to 10^9 GeV. NuGen generates the neutrinos on the surface of the Earth within a user specified zenith range, and propagates them to the detector volume while accounting for all relevant standard model processes including neutrino absorption, and deep inelastic scattering. The detector volume is modeled with a cylinder parallel to the neutrino direction, with a radius and height sufficiently large to account for the fact that IceCube is sensitive to neutrinos with an interaction vertex outside the detector. Once neutrinos reach the detector volume, they are forced to interact inside, and the actual interaction probability at that position is used for computing the weight:

$$w(E,\theta) = p_{int}\frac{A\Omega}{Np_{gen}(E)}\Phi_{target}(E,\theta) \tag{3.1}$$

where p_{int} is the probability of the interaction, $A = \pi r_{gen}^2$ is the area of the injection surface, N is the total number of injected events, p_{gen} is the probability of choosing a neutrino with the specified energy given the input spectra, and Φ_{target} is the flux being weighted to in units of $\mathrm{GeV}^{-1}\mathrm{cm}^{-2}\mathrm{s}^{-1}\mathrm{sr}^{-1}$. Φ_{target} takes on the value of the desired spectrum (i.e. atmospheric, astrophysical, or dark matter flux).

Once the simulated neutrinos are forced to interact in the detector, the resulting charged leptons and hadronic showers are handled by the "Proposal" particle propagator, which accounts for ionization losses, pair production, bremsstrahlung, and photonuclear interactions. The resulting photons from these secondary processes are propagated through the Spice-Mie ice model (discussed in Section 2.7) using the Photon Propagation Code (PPC) [74].

Once the simulated photons are propagated to the DOMs, they interact with the photocathode in the form of Monte Carlo photoelectrons (MCPEs). PMT noise is added in the form of additional MCPEs. For low energy analyses, understanding and properly accounting for this noise is extremely important since the noise can mimic low energy physics events. For this analysis, the noise was assumed to be of thermal origin, and was modeled as uncorrelated Poisson processes. Newer simulation software takes into account the thermal noise as well as radioactivity due to the potassium, thorium, and uranium in the glass [75]. The PMT response to the photons from the neutrino-induced processes, along with the PMT noise, and PMT efficiency are convolved to produce an analog waveform which is then digitized by the simulated ATWD/FADC, and triggers are applied exactly as described in Section 2.3 which results in simulated events.

The simulated events used for this analysis were generated with NuGen using an E^{-1} spectrum, and reweighted to represent the neutrino flux from atmospheric and astro-

physical sources, as well as the flux expected from gravitino dark matter decay.

3.2 Simulating Differential Neutrino Flux from Gravitino Decay

The neutrino spectra of the two-body gravitino decay modes were simulated with PYTHIA 6.4. The possible two-body decay channels for the gravitino include decay into a neutral boson (γ, Z^0, h^0) and a neutrino, or decay into a charged boson ($W^{\pm}$) and an accompanying lepton with opposite charge. The charged boson channels produce a continuous energy spectrum, while the neutral boson channels, with the exception of $\gamma\nu$, produce a continuous spectrum with a spectral line at the energy corresponding to the initial daughter neutrino. The $\gamma\nu$ channel simply produces monoenergetic neutrinos.

The simulation was performed using my code, based on [36], with helpful suggestions from the author. PYTHIA contains the usual three generations of neutrinos (ν_e, ν_μ, ν_τ), and also an unused 4th generation neutrino. This 4th generation neutrino was redefined to have a mass corresponding to the dark matter mass, and 100% branching into a specific decay channel. The simulation generated 10 million decays for each decay mode of a 2 PeV gravitino. A plot of the combined spectra for 150 GeV was produced (Figure 3.1(a)) for comparison to the literature [36], and to show the separation of the spectral lines from the individual decay modes. This result agrees well with [36] using the branching ratios listed therein ($\gamma\nu$: 1.1%, $W^+\tau^-$: 70%, $Z^0\nu$: 28%, $h^0\nu$: 1.2%).

For the h^0 channel, it was noted by Grefe that the h^0 should decay isotropically in its rest frame due to being a scalar, which doesn't happen in simulation. To work around this limitation, a particle beam was created with an energy equal to the dark matter mass, and the h^0 and accompanying neutrino were added as resonances. The results are shown in Figure 3.2.

The Monte Carlo simulation files used in this analysis were generated using an E^{-1} spectrum. The signal had to be reweighted to represent the actual neutrino flux that would result from gravitino decay. The reweighting was performed according to the equation for

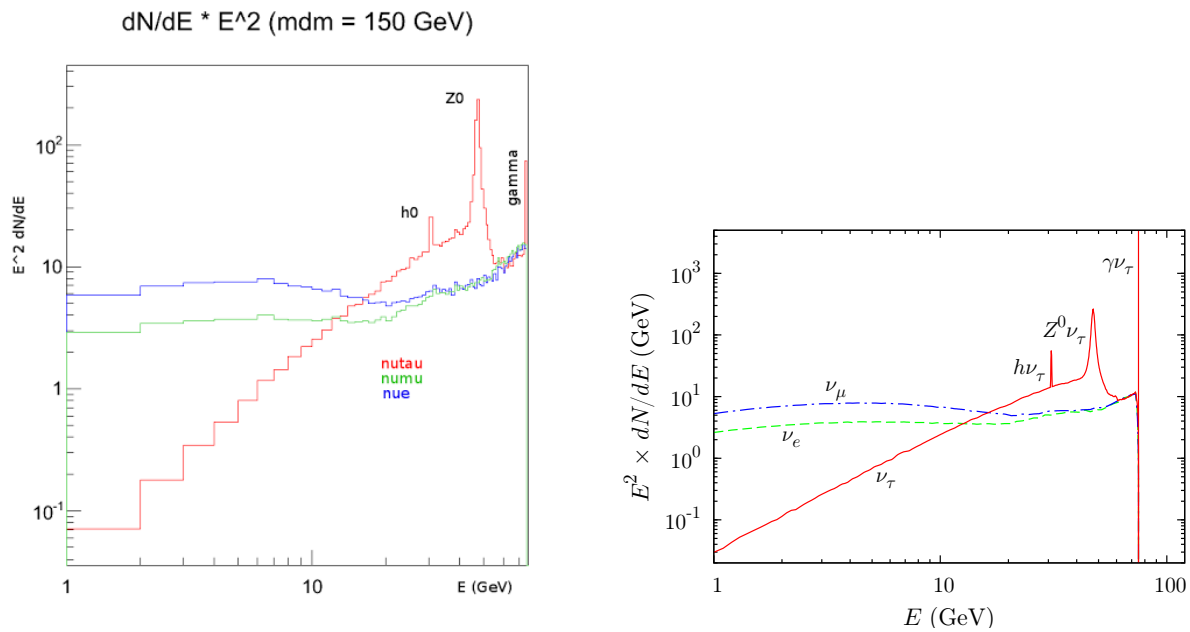

(a) (b)

Fig. 3.1.: Left: Simulated neutrino spectrum at IceCube produced by 150 GeV decaying gravitino dark matter assuming a lifetime of 10^{28} s and 100% branching into each decay mode. Right: Published spectrum from Grefe 2008 for comparison.

differential flux:

$$\frac{d\Phi}{dE} = \frac{1}{\tau}\frac{R_{sc}\rho_{sc}}{4\pi m_\chi} J(\psi)\frac{dN}{dE} \tag{3.2}$$

Where τ is the lifetime of the dark matter particle, and dN/dE is the differential neutrino flux. R_{sc} and ρ_{sc} represent the radius of the solar circle and the local dark matter density respectively and are used to create a dimensionless $J(\psi)$, the integral over the line-of-sight of the dark matter density ρ:

$$J(\psi) = \int_0^{l_{max}} \frac{\rho(\sqrt{R_{sc}^2 - 2lR_{sc}cos(\psi) + l^2})}{R_{sc}\rho_{sc}} dl \tag{3.3}$$

$$l_{max} = \sqrt{R_{MW}^2 - R_{sc}^2 sin^2\psi} + R_{sc}cos\psi \tag{3.4}$$

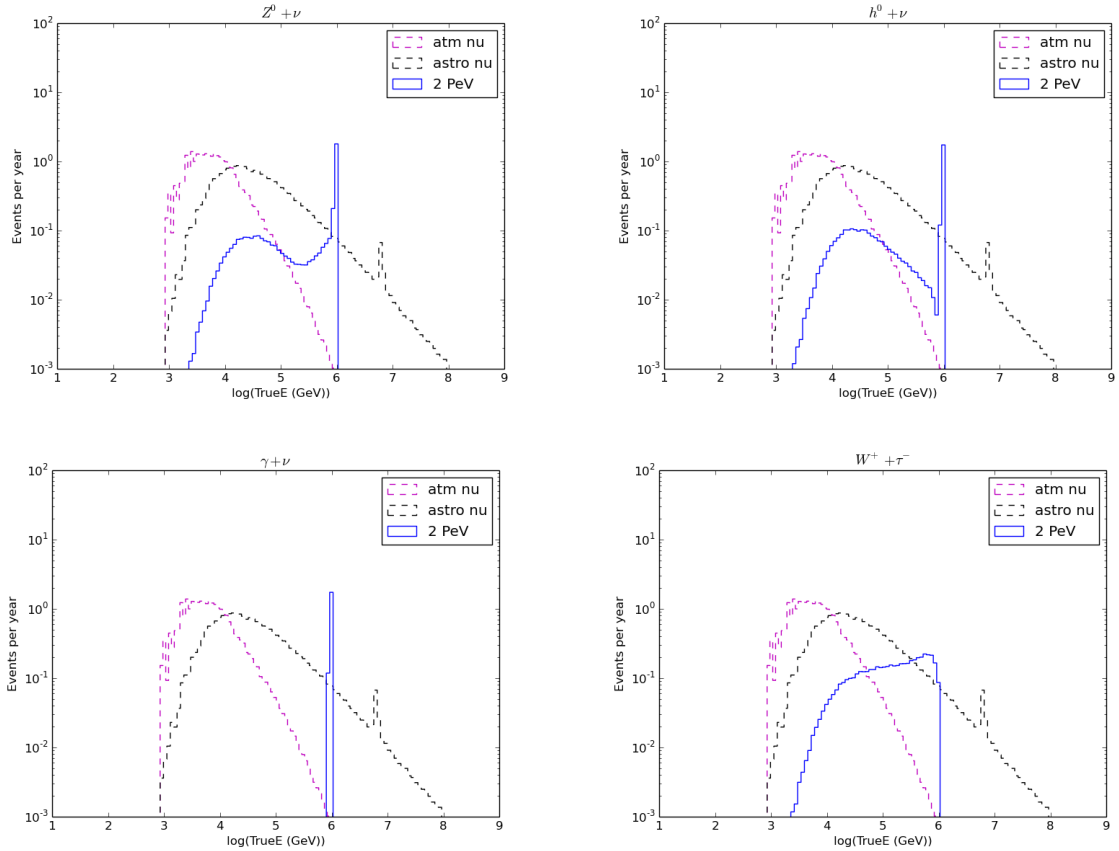

Fig. 3.2.: Energy spectra of the various gravitino two-body decay channels for a 2 PeV dark matter mass and lifetime of 10^{28}. The neutral boson channels show the distinct monoenergetic line at half the dark matter mass.

where R_{MW} represents a distance sufficiently far such that the contribution from the Milky Way halo at this distance can be neglected (40 kpc for this analysis). A diagram is provided in Figure 3.3 to show the relationship between l_{max}, R_{MW}, and R_{sc}.

In more detail, the $\frac{J(\psi)}{m_x}$ term represents the number density of dark matter particles, where $J(\psi)$ is the integral along the line-of-sight of the dark matter density. This term is divided by 4π to account for the isotropic emission of decay products. The $R_{sc}\rho_{sc}$ term cancels with the scaling factor used to make $J(\psi)$ dimensionless, and dN/dE is the differential neutrino flux associated with the decay of the gravitino. The differential neutrino flux was producing using PYTHIA 6 (Section 3.2).

For this analysis we use the Burkert dark matter profile, as parameterized in [22]

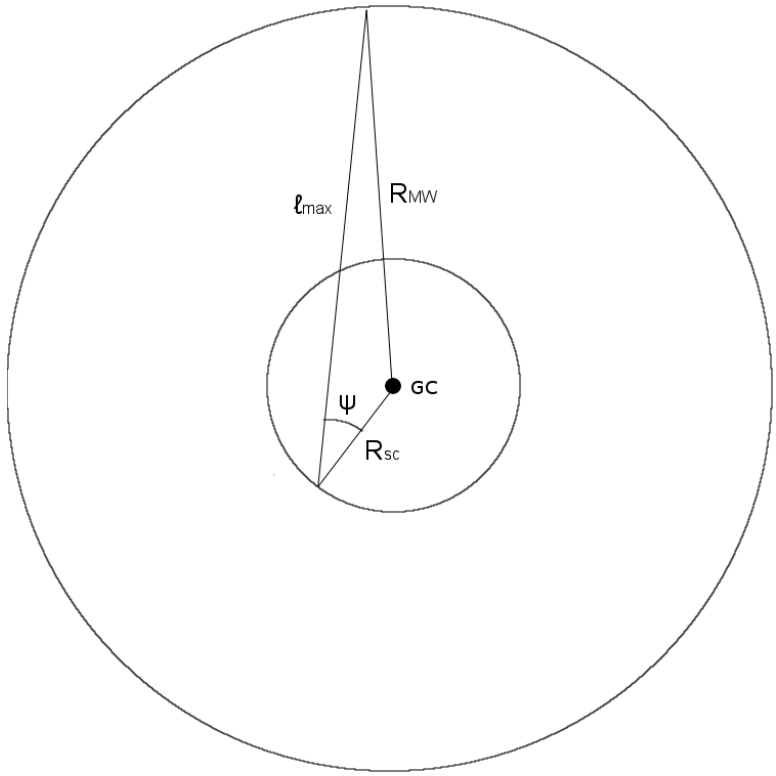

Fig. 3.3: Two dimensional illustration of the relationship between R_{sc}, R_{MW}, and l_{max} for an event with an angular distance ψ from the GC.

to model the matter distribution in the Milky Way:

$$\rho_{Bur} = \rho_H \frac{1}{(1+\frac{r}{R_H})(1+\frac{r^2}{R_H^2})} \tag{3.5}$$

where ρ_H and R_H are the scale density and scale radius respectively, and r is the distance from the center of the galaxy.

The neutrino flux from dark matter decay does not depend on dark matter density squared the way the flux from annihilation does, and thus the choice of halo profile has minimal effect on the resulting neutrino flux.

3.2.1 Propagation to Earth

The initial neutrino flavor composition from the decay is not directly observable. One has to account for neutrino oscillation over cosmic distances that result in an oscillation-

averaged flavor composition. A recently published IceCube analysis [76] measured the diffuse atmospheric flux and the findings are consistent with neutrinos arriving equally in all flavors ($\nu_e : \nu_\mu : \nu\tau = 1 : 1 : 1$). In particular, maximally track-like ($0 : 1 : 0$) and maximally shower-like ($1 : 0 : 0$) compositions are excluded to 3.3σ and 2.3σ respectively. For simplicity, we will assume in the following that each neutrino flavor in the gravitino decay spectrum at Earth carries 1/3 of the total flux ($1 : 1 : 1$), which is in agreement with [76].

3.2.2 "Smearing" the Neutrino Line

Due to the fact that only neutrinos with a very specific energy contribute to the spectral line, reconstructed quantities regarding the line suffer from inadequate statistics. In order to work around this, the assumption was made that a neutrino with $E_\nu = \frac{M_{DM}}{2}$ will behave similarly to neutrinos with energies between 95% and 105% of the original neutrino energy. This assumption allows the monoenergetic line to be "smeared" into energies around the spectral line. The wider range of energies now occupied by the line then yields more neutrino events for reconstruction variables such that they are less strongly affected by poorly reconstructed events.

For this analysis, my code converted the monoenergetic line to a Gaussian with a width of 5% of the dark matter mass. The height was scaled such that the total number of neutrinos produced from the decay remained the same. The effect of this smearing is shown below for the $Z^0 + \nu_\tau$ channel. This procedure is shown in Figure 3.4.

3.2.3 Spectrum at IceCube

Simulated events which pass the HESE selection were weighted to the flux from gravitino decay as outlined in Section 3.1 to get the rate of signal events at IceCube. The neutrino interaction cross sections, effective volume of the detector, and neutrino absorption by the earth are already accounted for in the simulation (Section 3.1).

A python module I wrote, called *dmweights*, was used to calculate the flux as a function of the angle around the galactic center. The module takes the direction of the incoming neutrino, calculates the angular distance from the galactic center and uses that value to calculate the line of sight integral (Eqn. 3.3) over the dark matter density profile for that angle. This value is then multiplied by the value of the differential spectrum calculated by PYTHIA ($\frac{dN}{dE}$), and scaled by the lifetime of the gravitino (Eqn. 3.2). In this way, each event in the simulation file is assigned a weight representing the expected flux of such an event if it were to be caused by gravitino decay. The spectrum at IceCube is shown in Figure 3.5 for a dark matter mass of 2 PeV and a lifetime of 10^{28}s.

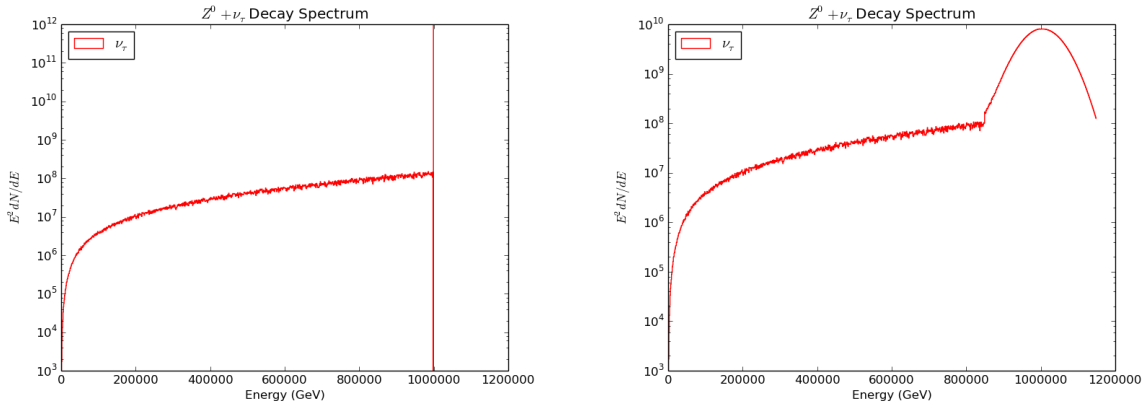

Fig. 3.4.: After smearing the height of the peak is reduced, and the original neutrino is "smeared" into surrounding energies in the form of a Gaussian with width of 5% of the dark matter mass.

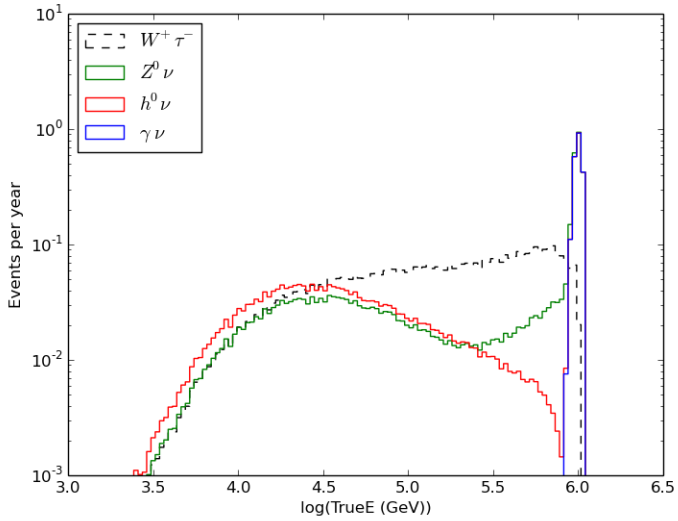

Fig. 3.5.: Neutrino spectrum at IceCube produced by 2 PeV decaying gravitino dark matter assuming a lifetime of 10^{28} s and 100% branching into each decay mode.

4 RECONSTRUCTION

In order to identify possible spectral features and an asymmetrical angular distribution expected from a gravitino signal, it is necessary to measure the energy and direction of the neutrino flux as accurately as possible. To this end, IceCube has many different methods of reconstructing the energy, position, and direction of the incoming neutrino from the timing and amount of light deposited in DOMs at various positions.

At energies at and above the TeV energy range, neutrinos primarily interact via deep-inelastic scattering, which produces a hadronic shower at the interaction vertex. Charged-current interactions, where a charged boson is exchanged, produce a hadronic shower accompanied by an outgoing lepton. This lepton can trigger an additional electromagnetic or hadronic shower in the detector, created by the outgoing electron, tau decay, muon brehmsstrahlung, and/or pair production.

In the TeV energy range, the amount of light deposited in the detector in a charged-current interaction is fairly consistent for a given energy and close to the original neutrino energy, since nearly all of the daughter particles produce visible light. For neutral current interactions, the energy deposited, and thus the light yield, can vary greatly based on the amount of energy carried away by the outgoing neutrino in the scattering process (Figure 4.1). At the energies considered in this analysis, the rate of neutral current interactions is roughly 3 times smaller than the rate of charge current interactions [78].

When considering only cascades, both types of interactions have similar shapes but vary in the amount of light deposited as a function of energy. The fact that both types of events have the same basic shape, coupled with the fact that the light deposited scales linearly with energy, allows for scaling a template cascade to the most likely energy which fits the data. This process takes into account the number of photons observed, propagation

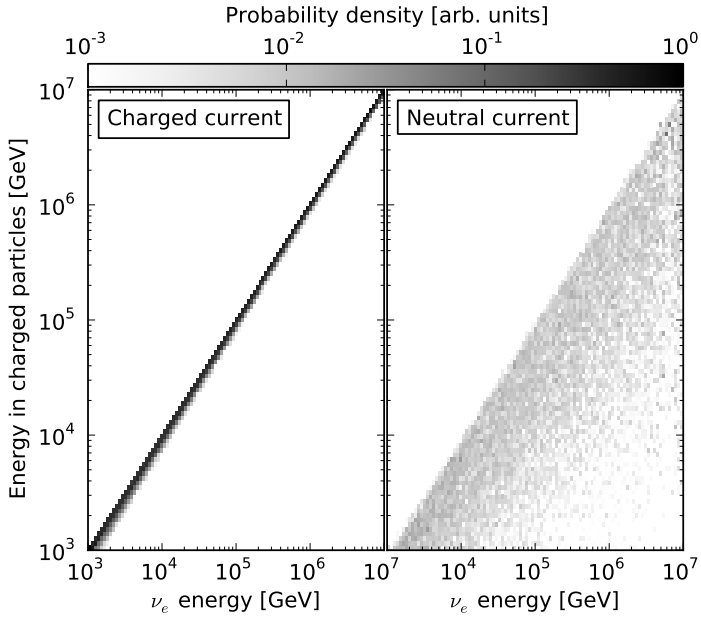

Fig. 4.1.: Energy of the Cherenkov radiating charged particles produced by charged (left) and neutral (right) current interactions. Charged current events deposit nearly all of their energy in the detector in the form of radiating particles, whereas neutral current interactions can deposit significantly less due to the high variability of the outgoing neutrino energy [77].

through the ice, detector response, and the light expectation value from a template Monte Carlo cascade.

The number of photons measured by the PMTs follows a Poisson distribution around a mean: $\lambda = \Lambda E$, where Λ is the average number of photons detected per unit energy. Thus,

Interaction	Signature	E_{vis}/E_ν; $E_\nu = 1$ TeV	$E_\nu = 10$ TeV	$E_\nu = 100$ TeV
$\nu_e + N \to e + had.$	Cascade	94%	95%	97%
$\nu_\mu + N \to \mu + had.$	Track (+ Cascade)	94%	95%	97%
$\nu_\tau + N \to \tau + had. \to had.$	Cascade/Double Bang	$< 94\%$	$< 95\%$	$< 97\%$
$\nu_\tau + N \to \tau + had. \to \mu + had.$	Cascade + Track	$< 94\%$	$< 95\%$	$< 97\%$
$\nu_l + N \to \nu_l + had.$	Cascade	33%	30%	23%

Table 4.1.: The ratio of the median visible energy deposited in the detector to the energy of the incoming neutrino as a function of the interaction type.

the likelihood ($\mathcal{L}$) for k detected photons with an event of energy E is:

$$\begin{aligned} \mathcal{L} &= \frac{\lambda^k}{k!}e^{-\lambda} = \frac{(\Lambda E)^k}{k!}e^{-\Lambda E} \\ \Rightarrow \ln \mathcal{L} &= k\ln(\Lambda E) - \ln(k!) - \Lambda E \end{aligned} \tag{4.1}$$

Generalizing to include photons from noise in the PMT (ρ) leads to:

$$\ln \mathcal{L} = k\ln(\Lambda E + \rho) - \ln(k!) - (\Lambda E + \rho) \tag{4.2}$$

The average number of photons, Λ, is obtained from a spline table assembled from Monte Carlo simulations of interactions in various parts of the detector. The spline table is parameterized by six properties of an event: the depth at which the interaction takes place, its zenith angle, the three distance variables (x, y, z) measured from the event to the DOM, and the time difference between light being emitted and when it is observed in the detector [79]. These tables are around 1 GB in size and a single lookup takes around 1μs. Minimization algorithms use this information to find the energy associated with the minimum negative log-likelihood ($E_{bestfit}$) for an event. Although typical shower sizes (Figure 4.2) are not resolvable with IceCube's DOM spacing (17m vertical, 125m horizontal), photons are still peaked at the Cherenkov angle. The particles produced in the shower quickly lose their energy via bremsstrahlung radiation, but directional information can still be obtained, and thus fit, using the timing of the hit pattern.

In the case of charged-current interactions the reconstructed energy is approximately equal to the energy of the incoming neutrino ($E_{bestfit} \approx E_\nu$), while for neutral current interactions it is simply a lower bound on the neutrino energy ($E_{bestfit} < E_\nu$). Since only two out of three neutrino interactions (ν_e CC, ν_τ CC) result in a reconstructed energy approximately equal to the neutrino energy, about half of the events with energies corresponding to a spectral line can be expected to contribute to the line in the reconstructed energy.

The specific reconstruction used in this analysis started with a basic line fit, using

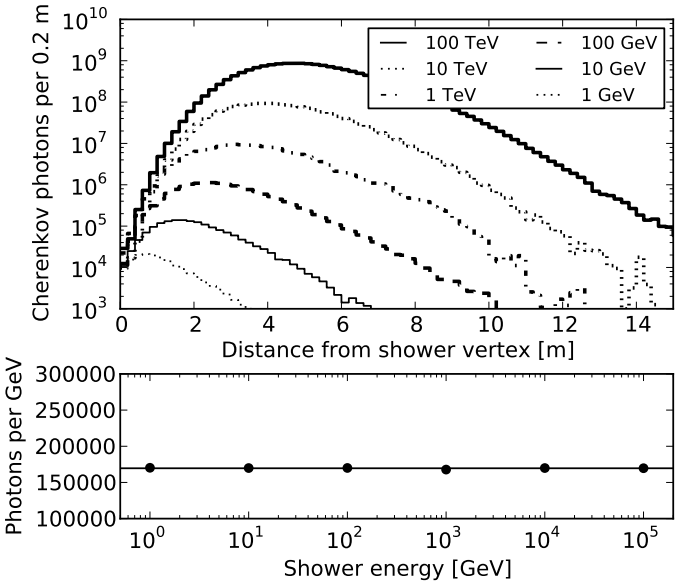

Fig. 4.2.: The top plot shows GEANT simulation of the average number of Cherenkov photons emitted in ice as a function of longitudinal distance from the interaction vertex of an electromagnetic cascade [80]. These are, in general, too small to be resolved with IceCube's DOM spacing. The bottom plot shows the photons emitted per GeV, which illustrates that the number of photons scales linearly with shower energy.

the timing of the first pulse detected by each DOM. The relationship of the DOM position ($\vec{x}_{DOM}$) to the particle position and velocity is given by

$$\vec{x}_{DOM,i} = \vec{x_0} + t_i \cdot \vec{v}$$

This can be solved analytically by:

$$\vec{x_0} = \langle \vec{x}_{DOM,i} \rangle - \vec{v}_{LineFit} \langle t_i \rangle$$

and

$$\vec{v}_{LineFit} = \frac{\langle t_i \cdot \vec{x}_{DOM,i} \rangle - \langle \vec{x}_{DOM,i} \rangle \langle t_i \rangle}{\langle t_i^2 \rangle - \langle t_i \rangle^2}$$

where $\langle x \rangle$ is the arithmetic mean for all pulses and DOMs in the event [81].

The line returned by this fit is used as the seed to a more sophisticated infinite track reconstruction algorithm. The track reconstruction is based on empirical data using laser light signals at the BAIKAL experiment [82]. Only the first light arrival time for each DOM is used in constructing the p.d.f. This algorithm fits a track along randomly chosen directions and minimizes the negative log-likelihood to find the best fit track hypothesis.

Next, a cascade reconstruction algorithm is used that is based on the same empirical arrival times as in the track reconstruction, but now using a point source emitting hypothesis. The cascade reconstruction is seeded with the previous best fit track hypothesis under the assumption that the cascade vertex lies somewhere along the track. For each point along the track, a cascade hypothesis is used to calculate a likelihood, and similarly to the track fit, minimization of the negative likelihood gives a best fit cascade vertex position, direction, and energy.

The final step in the reconstruction chain involves using the tabulated light yields from a simulated 1 GeV electromagnetic cascade. The deposited energy is determined by scaling the template to best match the charge collected in each of the DOMs. This

template is obtained from the 5-dimensional spline surface referenced in Equations 4.1 and 4.2. Energy, direction, and position variables are fit simultaneously to return the best fit values.

5 ANALYSIS

This analysis applies the same event selection as in [43, 44]. This event selection is known as the High Energy Starting Event (HESE) selection. No more than three photoelectrons out of the first 250 must be in the veto region, as described in [43]. This veto region (Figure 5.1) includes the top 90m, bottom 10m, and outermost strings of the detector as well as a region of high dust concentration from 2000m to 2100m, known as the "dust layer" (Figure 5.1). Additionally, the event must also produce at least 6000 p.e. to ensure (to 99.999%) that cosmic ray muons would produce enough light in the veto region to be excluded.

To ensure the event selection for this analysis was identical to [44], it was applied to simulation files containing neutrinos of all flavors. The atmospheric rates were calculated for various models using the simulation datasets from the original HESE paper[43]. HESE estimates of the atmospheric flux were based on [62] with corrections from [63], and led to 6.6 events in 988 days with ERS fit to 0. After analyzing 100 files from each of their datasets, there is good agreement (2.584/yr) with HESE ($2.43^{+2.18}_{-0.59}$/yr).

This analysis uses the same conventional atmospheric flux model as in [44] and yields a rate of 3.54 atmospheric events year. However, the prompt flux was modeled as described in [66] and corresponds to the upper limit quoted in the published results of [44]. Including the upper limit in the prompt flux as part of the background provides a conservative limit on the dark matter lifetime and decreases the likelihood of interpreting the prompt flux as a dark matter signal. The astrophysical power law fit to the published flux resulted in 9.6 events per year, leading to a total event rate of 13.14 events per year. The average event rate over 3 years of data is 13.7/yr [44].

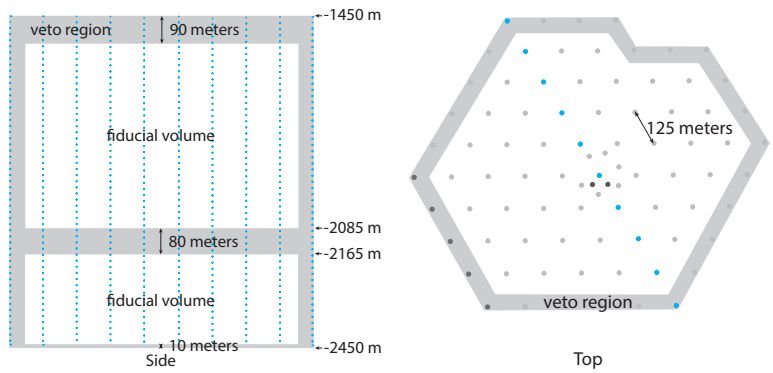

(a) Side view of the veto region (b) Top down view of the veto region

Fig. 5.1.: Veto region used in this analysis as well as in the published results[44] which includes the top 90m, bottom 10m, and outermost strings of the detector as well as the dust layer.

5.1 Reconstruction

In order to test the accuracy of the reconstruction procedure used in this analysis, it was tested on simulation files of all flavors of neutrinos. These events were reweighted from an E^{-1} spectrum, to the spectrum expected from gravitino decay following the procedure outlined in Chapter 3. After reweighting, the reconstruction procedure outlined in Chapter 4 was performed on the newly weighted files. The results are shown in Figures 5.1 and 5.2.

In order to test the average performance of the reconstruction algorithm for the gravitino decay mode spectra, the reconstructed values were compared to the Monte Carlo truth values, and the standard deviation of the differences is quoted as the resolution. The energy resolution of the reconstruction is listed for each decay mode in Figure 5.2 and the azimuth and zenith resolutions are shown in Figure 5.3. The $\gamma\nu$ spectrum resolution was 0.136 in $log(\frac{TrueEnergy}{RecoE})$, which amounts to the true energy being 36% larger on average than the reconstructed energy. This effect is due to the inclusion of neutral current events, where the scattered neutrino carries away energy from the detector. This effect is discussed in Chapter 4 and shown in Figure 4.1.

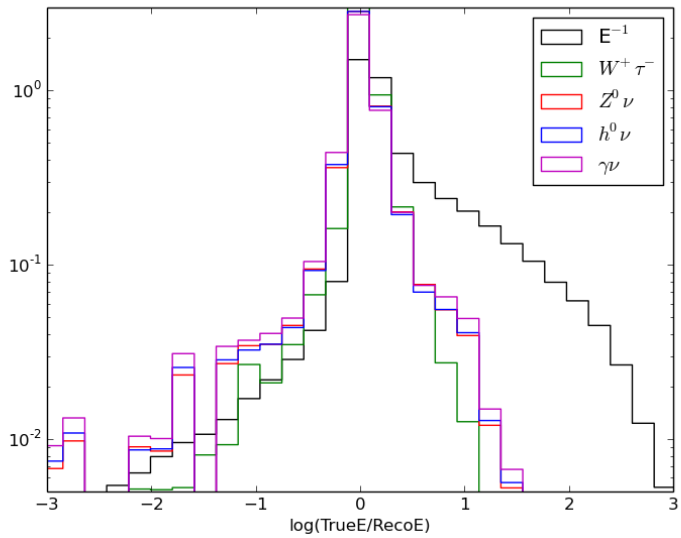

Weighting	Mean Resolution	Std. Dev.
E^{-1}	0.529	0.943
$W^+\tau^-$	0.088	0.309
$Z^0\nu$	0.094	0.435
$h^0\nu$	0.102	0.442
$\gamma\nu$	0.136	0.554

Fig. 5.2.: Energy Resolution - Mean and Std Dev in log(GeV)

In the IceCube 2-year published results [43] events were reconstructed by dividing the sky into pixels and fixing the direction in the fitting algorithm. A separate reconstruction was run for each pixel, to create a likelihood map. The primary reason for such an intense reconstruction algorithm was to prevent the fitter from getting stuck in a local minimum. This brute force method of reconstruction was not suitable for this analysis due to the use of simulation files containing hundreds of thousands of events, as opposed to the 28 events in the 2 year publication. Additionally, the current reconstruction algorithms have improved since the time of the publication (2013). The reconstruction results for this analysis are shown side by side with the published results in Table 5.3. The differences are all within 1σ of the resolution.

The size of the angular bins is based on the direction resolution, and is set at 60 degrees. Only one of the events falls outside of this range. The last event shows the

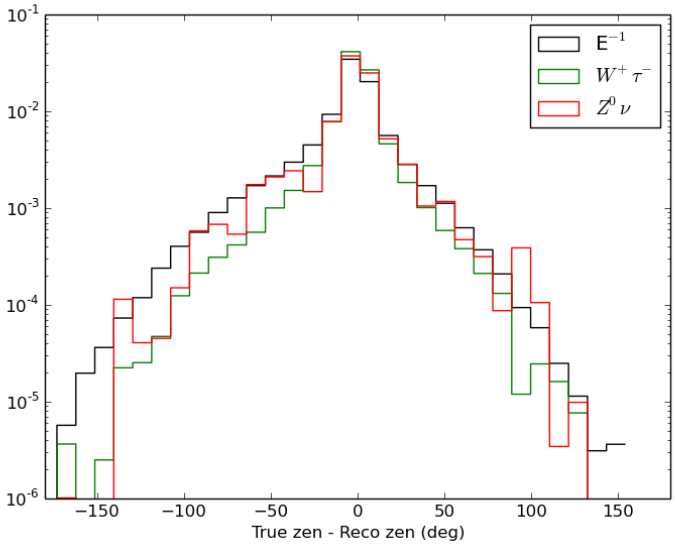

Weighting	**Mean Resolution**(°)	**Std. Dev.**(°)
E^{-1}	-4.98	26.44
$W^{+}\tau^{-}$	-1.39	17.92
$Z^{0}\nu$	-2.22	23.82
$h^{0}\nu$	-2.19	23.60
$\gamma\nu$	-2.52	25.49

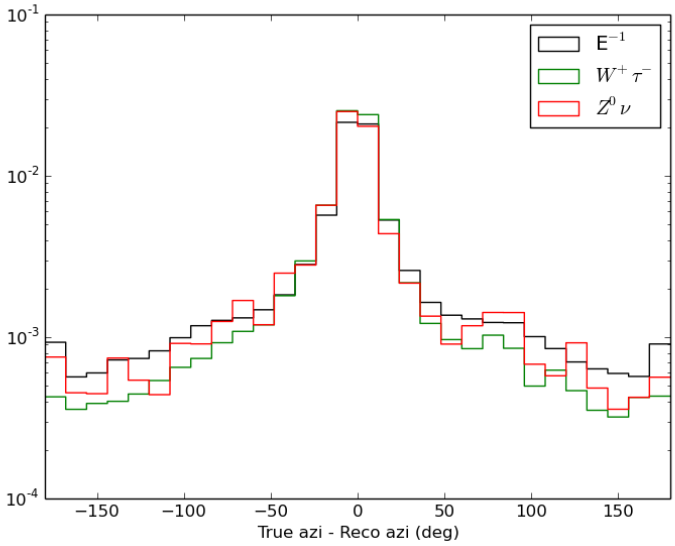

Weighting	**Mean Resolution**(°)	**Std. Dev.**(°)
E^{-1}	-0.54	57.32
$W^{+}\tau^{-}$	-1.11	45.49
$Z^{0}\nu$	-2.17	52.88
$h^{0}\nu$	-1.93	52.22
$\gamma\nu$	-2.37	54.65

Fig. 5.3.: Angular Resolution for zenith (top) and azimuth (bottom) angles. Mean and standard deviations listed in degrees

largest deviation in angle from the HESE two year results. This analysis uses a cascade reconstruction algorithm, which performs well on most tracks, but this last event was a track near the bottom of the detector with only a few hits as it left the detector (as shown in Figure 5.4. This is likely the cause of the poor direction reconstruction. The event shows good agreement in declination, but differs by 147.9 degrees in right ascension.

Although the NFW halo profile accurately describes dark matter halos produced in large computer simulations [27], the Burkert profile was chosen for this analysis because it is a better fit to halo densities calculated from stellar velocities in low surface brightness galaxies [83]. A comparison of the effect of different halos is shown in Section 5.3.9.

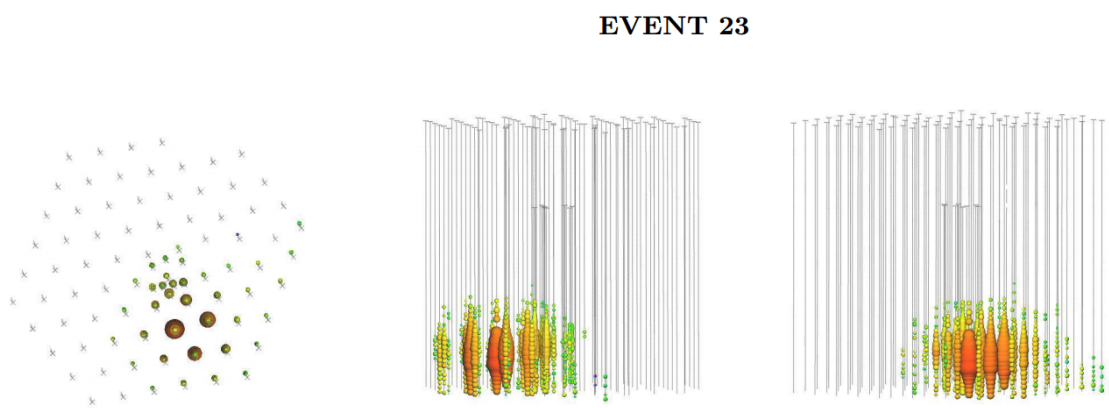

Fig. 5.4.: Event 23 from the published results[44]. This event differs most from the published results in direction reconstruction due to the fact that the track exited the detector with only a few hits, which a cascade reconstruction algorithm is less sensitive to.

Decay Mode	True Energy	Reconstructed Energy
$W^+\tau^-$	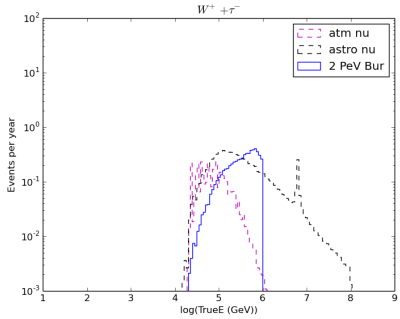	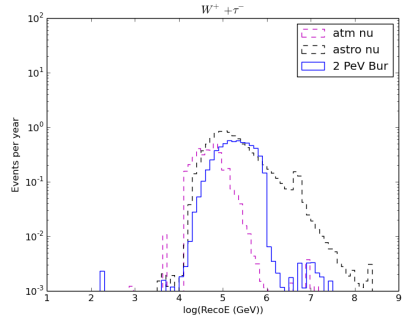
$Z^0\nu$	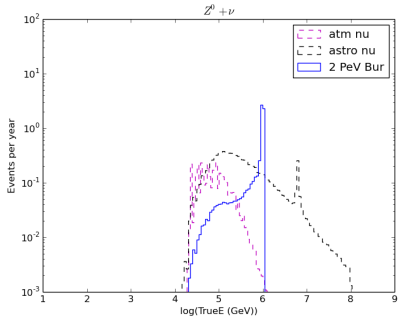	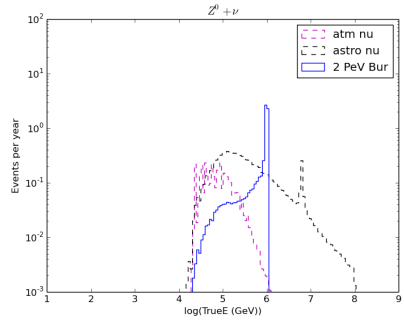
$h^0\nu$	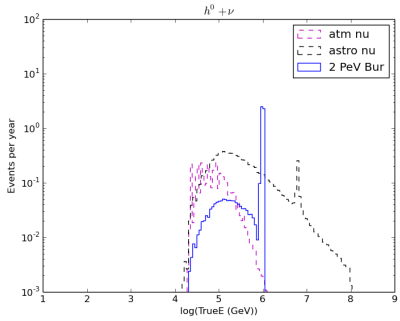	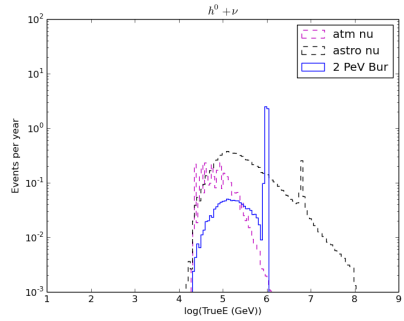
$\gamma\nu$	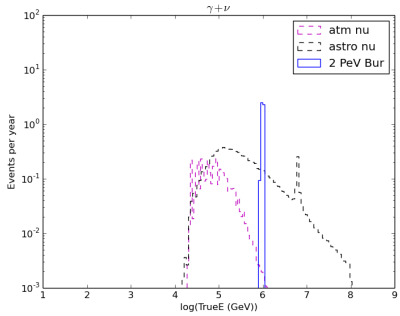	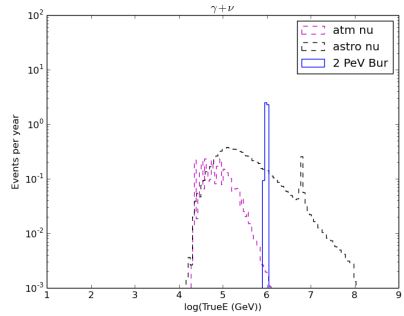

Table 5.1.: True energy and reconstructed energy plots for each of the gravitino decay modes considered in this analysis. The peak at 6.3 PeV corresponds to the Glashow resonance described in Section 2.5.3.

Decay Mode	True Direction	Reconstructed Direction
$W^+\tau^-$	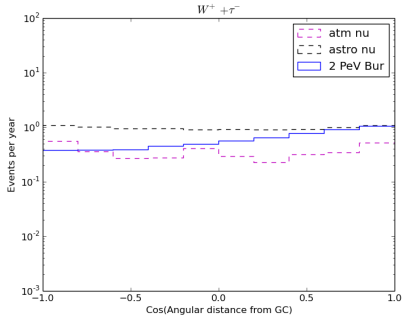	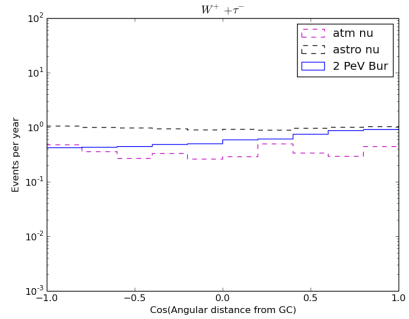
$Z^0\nu$	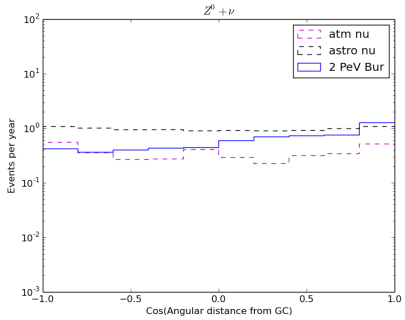	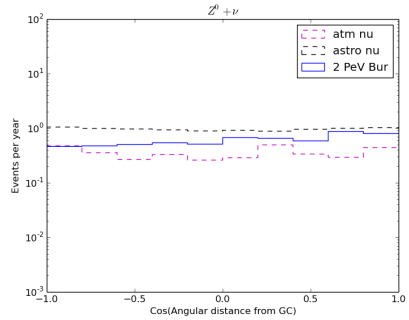
$h^0\nu$	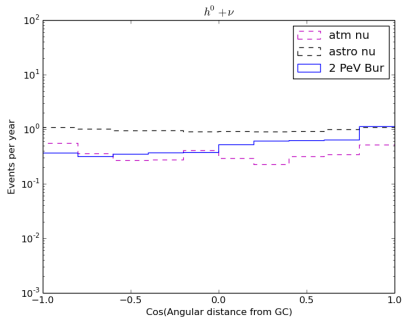	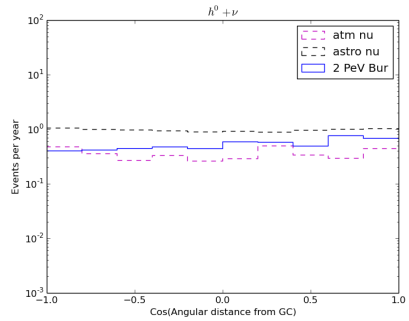
$\gamma\nu$	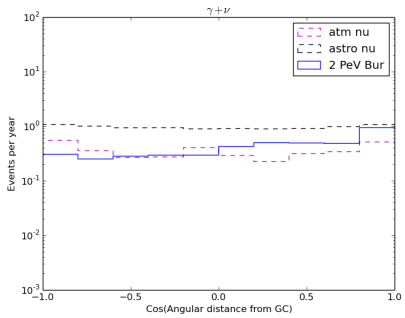	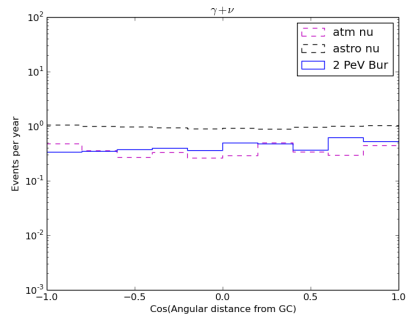

Table 5.2.: True direction and reconstructed direction plots for each of the gravitino decay modes considered in this analysis using a Burkert halo profile.

MJD	**My RA**	**Published RA**	**My Dec**	**Published Dec**	**Type**	**ΔAngle**($^\circ$)
55695	9.6	5.0	-4.7	-29.4	Shower	24.7
55714	159.0	155.3	-7.4	-8.9	Shower	1.6
55739	265.5	296.1	-56.4	-52.8	Shower	25.1
55756	79.3	67.9	23.2	40.3	Track	18.1
55782	260.1	265.6	-36.2	-27.9	Shower	8.8
55783	271.7	287.3	-50.9	-49.7	Shower	12.0
55798	250.4	192.1	-27.0	-22.6	Shower	23.9
55800	263.7	247.4	22.1	14.5	Shower	9.1
55923	3.2	345.6	-12.0	-24.8	Track	13.8
55925	91.5	76.9	-63.2	-59.7	Shower	13.3
55929	338.3	38.3	-61.1	-67.2	Shower	53.8
55936	54.3	9.0	-24.5	-24.0	Shower	18.2
55941	289.5	293.7	-21.1	-22.1	Shower	1.8
55949	109.3	208.7	23.4	-13.2	Track	24.7
55950	281.2	282.2	-19.6	-15.1	Shower	4.5
55966	61.2	286.0	-6.7	-14.5	Shower	19.8
55979	123.3	143.4	35.5	22.7	Shower	16.0
56008	137.1	121.7	-35.9	-12.6	Shower	24.0
56048	312.7	164.8	-76.4	-71.5	Track	134.9

Table 5.3.: Directional reconstruction comparison to HESE paper [43]

5.2 Likelihood Method

For this analysis, my python software implemented a likelihood method for setting a limit on the lifetime of the decaying dark matter. For a given three-dimensional histogram of data in reconstructed energy and direction, the probability of it having been produced by a given hypothesis can be calculated from the three-dimensional histogram of the hypothesis by calculating the Poisson probability of occurrence for each bin. The likelihood is then the product of the probabilities from each individual bin, representing the total probability that the data was produced by the hypothesis.

For an observable (O) with an expected value λ, the probability of measuring $O = k$ is given by the Poisson distribution:

$$Pr(O = k) = \frac{\lambda^k}{k!} e^{-\lambda} \tag{5.1}$$

In a binned-likelihood analysis, the value in each bin is compared to its expected value from simulation. The likelihood is then calculated by multiplying the Poisson probability of occurrence for each bin:

$$\mathcal{L} = \prod_{bin=1}^{nbins} P_{bin} \tag{5.2}$$

The best fit then is the hypothesis which produces the maximum likelihood.

In order to calculate the sensitivity, for each pseudoexperiment, the best fit background-only hypothesis was compared to the best fit background+signal hypothesis using the test statistic from Wilks' theorem:

$$\Lambda = \frac{\mathcal{L}_{sig+bg}}{\mathcal{L}_{bg}} \tag{5.3}$$

$$TS = -2\ln(\Lambda) \tag{5.4}$$

For this analysis, three likelihoods are considered (described below). For each likelihood, Poisson fluctuated pseudodata were generated representing background only sources as well as background plus a given dark matter signal. A total of 1000 pseudoexperiments were carried out for each of the two scenarios (bg only, sig+bg). For each pseudoexperiment, a test statistic was calculated. This resulted in a distribution of test statistics for background-only pseudodata as well as a distribution of test statistics for background with injected signal. If 90% of the signal+bg TS distribution is above the median of the background-only TS distribution, the detector is said to be sensitive that signal.

All likelihoods are computed from a 3D histogram of reconstructed energy, right ascension, and declination. The three likelihoods considered in this analysis differ only in their representation of the background.

Likelihood 1: In the first likelihood method, a power law is fit to the astrophysical flux: $\Phi_{astro} \propto E^{-2.3\pm0.3}$ is considered to be the background along with neutrinos produced in the atmosphere. The astrophysical flux was allowed to vary within the HESE uncertainties to result in the best fit. This interpretation leads to a sensitivity/limit for the case where none of the events were caused by dark matter decay.

Likelihood 2: For the second method, the astrophysical background is assumed to be a power law with an unknown spectral index and normalization. This background is then allowed to take on the values which lead to the best fit. This interpretation allows for events to have been created by both the astrophysical flux as well as dark matter decay, and sets the sensitivity/limit accordingly.

Likelihood 3: The third likelihood considers only atmospheric background, and 100% of the events detected are assumed to be from dark matter decay. This results in the most stringent limits on the lifetime of the dark matter. The results of each likelihood are presented in detail in the following section.

The bin sizes in reconstructed energy and direction were set equal to the mean resolution for each quantity (shown in Figures 5.2 and 5.3). This corresponds to bin sizes

of 0.44 in log(E) and 32 degrees for the angular distance from the galactic center (GC).

5.3 Sensitivity Calculation Procedure

To calculate the sensitivity of this analysis for various decay modes for a 2 PeV gravitino, a series of pseudoexperiments were conducted based on simulation data that represented the possible outcomes of a measurement. In order to generate pseudodata for each pseudoexperiment, a 3-dimensional histogram was created from the reconstructed energy, azimuth, and zenith of simulated neutrino events, which were weighted to represent the actual background and signal spectra.

The simulated 3-dimensional histogram was binned in each dimension according to the reconstruction resolutions shown in Figures 5.2 and 5.3. Using the value in each bin as the expected event rate, a pseudodata histogram was created with each bin value being chosen at random from a Poisson distribution with a mean equal to the original histogram bin value. The new histogram populated with pseudodata represented a possible outcome of the experiment.

5.3.1 Pseudodata Generation

Pseudodata is generated from creating a 3d histogram from the reconstructed energy, azimuth, and zeniths from simulation. Poisson fluctuations of the reconstructed 3d histogram is used to create pseudodata that represents one possible outcome of this experiment. Pseudodata is shown in Figure 5.5 for astrophysical and atmospheric backgrounds, and in Figure 5.6 for each decay mode with a dark matter lifetime $\tau = 10^{28}$ s. The plots are binned in cos(zenith) so that each bin represents equal area on the sky. The example plots are integrated over all energies to make visualization easier. An excess of events can be seen in the direction of the GC (RA = 17h 45m, cos(zenith) = 0.485).

For each likelihood method, the lifetime sensitivities and test statistic distributions are shown in Sections 5.3.3, 5.3.4, and 5.3.5. Although the background and signal dis-

tributions behave as expected, 2D histograms are shown in Figure 5.7 to illustrate the normal behavior of the pseudodata for signal and background. The first two figures show well behaved background and background with signal. The background sources are concentrated in the middle energy bins, whereas the signal occupies the highest energy bins. A pseudodata outlier is also shown, which had no dark matter events injected, but still scored a fairly high test statistic due to random fluctuations in the higher energy bins. These cases were expected, and are rare as shown in the test statistic distributions in the Sections 5.3.3, 5.3.4, and 5.3.5.

Ten thousand pseudoexperiments were generated using only atmospheric and astrophysical neutrinos. The atmospheric rates were based on [62], and the astrophysical rates were taken from the published IceCube measurement in [44]. Each background-only pseudoexperiment was fit using a background-only hypothesis to find the best fit parameters corresponding to the maximum likelihood ($\mathcal{L}_{bg-only}$). The same data were then fit using signal as well as background sources ($\mathcal{L}_{sig+bg}$). By performing a log-likelihood ratio test ($\ln \frac{\mathcal{L}_{sig+bg}}{\mathcal{L}_{bg-only}}$), it was possible to see how much more a background with signal hypothesis was

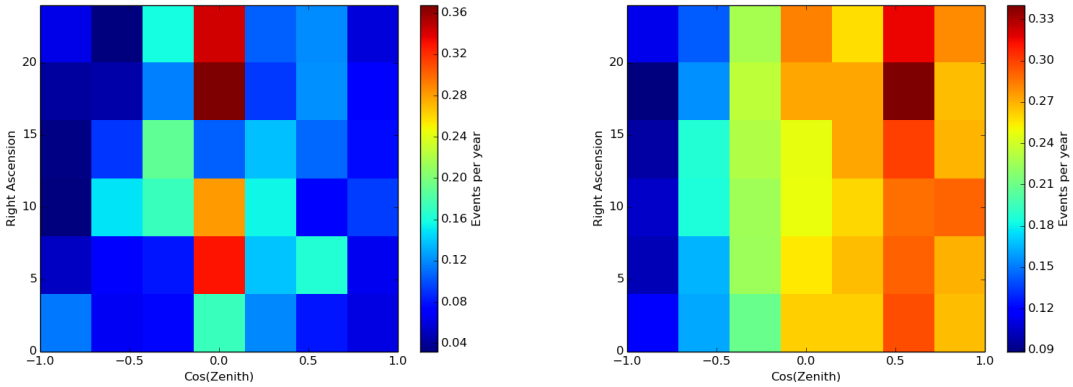

(a) Atmospheric flux - shows a peak at Cos(Zenith) = 0, consistent with the HESE 2yr results [44].

(b) Astrophysical flux (HESE 3yr powerlaw fit)

Fig. 5.5.: Atmospheric and astrophysical distributions in terms of Right Ascension and Cos(Zenith).

favored over a purely background hypothesis for a given pseudoexperiment. In the case of pseudodata created from background only sources, the result of the likelihood ratio gave insight into how well background sources could mimic a signal.

The same procedure was carried out for 1000 pseudoexperiments produced from background sources with injected signal events corresponding to a given dark matter lifetime and decay mode. The data were fit twice like the background only pseudodata. The first fit used only background sources, and the second used background and signal sources. The log-likelihood ratio distribution for the 1000 trials were plotted against the 10,000 background-only trials. The separation of these two distributions were compared to deter-

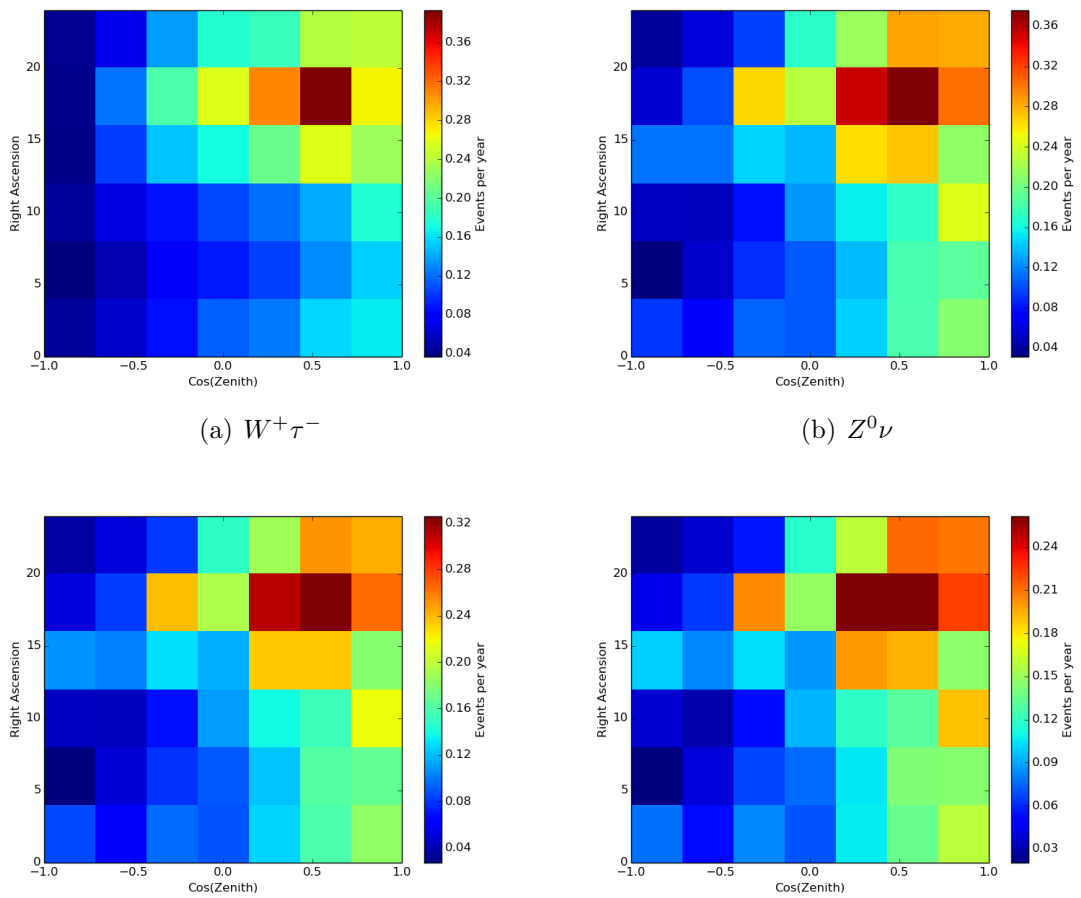

(a) $W^+\tau^-$ (b) $Z^0\nu$

(c) $h^0\nu$ (d) $\gamma\nu$

Fig. 5.6.: Signal distributions in terms of Right Ascension and Cos(Zenith). An excess from the GC is seen in the upper right hand corner of the plots.

mine the sensitivity of the analysis. If 90% of the background plus signal distribution was above the median of the distribution corresponding to the background-only sources, then the analysis was sensitive to the injected dark matter lifetime at the 90% confidence level. These distribution plots for the 90% sensitivity dark matter lifetimes are shown in Figures 5.8-5.10.

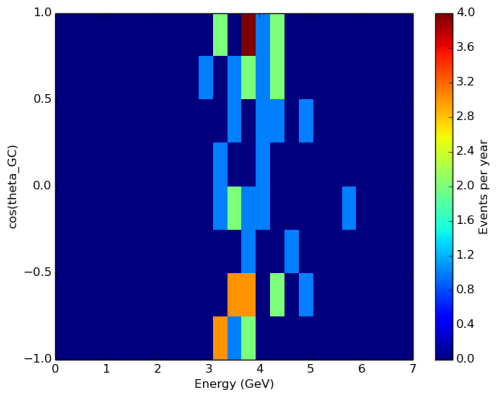

(a) Background-only: Behaves as expected, with majority of events at lower energies

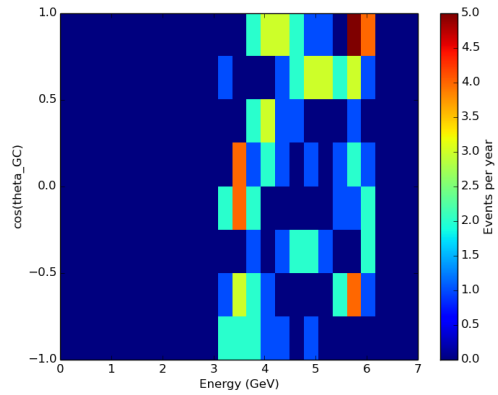

(b) Background + signal: Signal is apparent in the higher energy bins

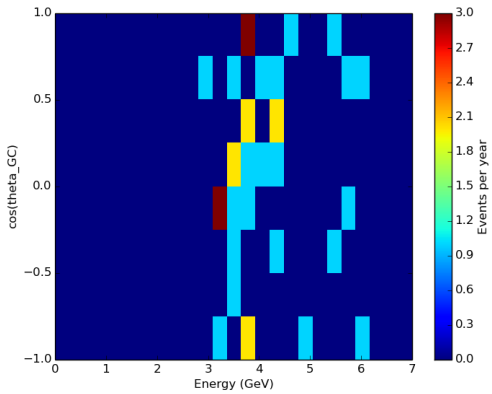

(c) Background-only Outlier: Random fluctuations in the higher energy bins lead to it to being scored as signal-like

Fig. 5.7.: Pseudodata examples for Z0 decay mode with lifetime $\tau = 10^{28}$ s

5.3.2 Fitting To Find The Maximum Likelihood

Once the 3D histogram is populated with pseudodata, the likelihood is calculated as a function of the astrophysical normalization, astrophysical spectral index, and dark matter normalization. The dark matter normalization corresponds to the inverse of the lifetime, and is used so that the dark matter contribution can be set to zero, rather than having arbitrarily long lifetimes that approach a infinitely small dark matter flux.

To optimize the speed of the fitting, the 3D histograms are created using the numpy Python package. Numpy uses FORTRAN libraries for multidimensional arrays, and can quickly perform numerical operations on the entire array. In this case, that corresponds to calculating the Poisson probabilities bin-by-bin between the pseudodata and that predicted by the input parameters.

The negative of the likelihood function is minimized using Minuit[84], a tool developed at CERN for finding the minimum of a multi-parameter function. The Minuit MIGRAD function uses the DavidonFletcherPowell formula, which is a multidimensional generalization of the secant method for finding stationary points of a function. In this method, a secant line is plotted between two points along the function in question $(f(x_1), f(x_2))$. The function is then reevaluated at the root of this secant line (x_3) and a new secant line is plotted between $f(x_2)$ and $f(x_3)$. If positive-definiteness is ensured, then repeated iterations will approach a minimum value of the function.

To increase the robustness of the fit, and to prevent the minimizer from getting "stuck" in local minima, the fit is performed ten different times each with a different order of magnitude seed for the dark matter normalization. The minimum negative likelihood from the ten fits is then taken as the best fit.

5.3.3 Sensitivity for Method 1 - Astrophysical spectral index allowed to vary within HESE 2yr uncertainty

The test statistic distributions shown in the following sections corresponds to the longest dark matter lifetime with at least 90% of its test statistic distribution above the median of the background-only distribution. As expected, the decay modes with spectral lines perform better. The astrophysical spectrum was weighted using the published HESE results $\Phi(E) = 1.5 * 10^{-8} E^{-2.3} (100 \text{ TeV})^{0.3} \text{GeV}^{-1} \text{cm}^{-2} \text{s}^{-1} \text{str}^{-1})$. For the first likelihood method, the test statistic distributions corresponding to the sensitivity and median best fit parameters from the likelihood fitter are shown in Figure 5.8.

5.3.4 Sensitivity for Method 2 - Astrophysical spectral index and normalization allowed to vary without bounds

For the second likelihood method, the sensitivities are only slightly worse than those from the first likelihood method. This is expected behavior because the astrophysical spectrum can soften to account for the lower energy events, while adding in dark matter to explain the higher energy events. The input astrophysical spectrum was weighted using the HESE results ($\Phi(E) = 1.5 * 10^{-8} E^{-2.3} (100 \text{ TeV})^{0.3} \text{GeV}^{-1} \text{cm}^{-2} \text{s}^{-1} \text{str}^{-1}$), but the fitter was allowed to vary the index and normalization. The test statistic distributions corresponding to the sensitivity as well as the median best fit parameters from the likelihood fitter are shown in Figure 5.9.

5.3.5 Sensitivity for Method 3 - Purely Atmospheric Background

As expected, the decay modes with spectral lines perform better. The test statistic distributions are larger because the background in this case is only the few atmospheric events that pass the HESE veto. Thus, the signal is harder to fit with a background only hypothesis leading to large values of the test statistic. The sensitivities and median best

fit parameters from the likelihood fitter are shown in Figure 5.10.

5.3.6 Effects of Binning

The effect of various bin sizes were tested and the effect on sensitivity was found to be minimal. As a sanity check, the sensitivity was calculated using 2 bins each for energy and direction, and the sensitivity was greatly reduced as expected. The test statistic

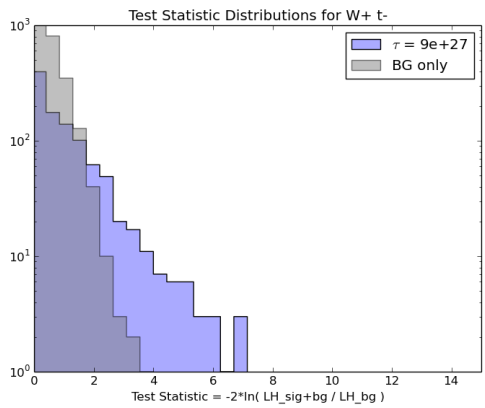

(a) $W^+\tau^-$ TS distribution for $\tau = 10^{27.95}$ s

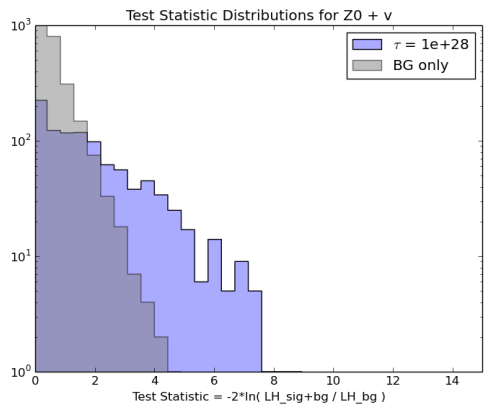

(b) $Z^0\nu$ TS distribution for $\tau = 10^{28.0}$ s

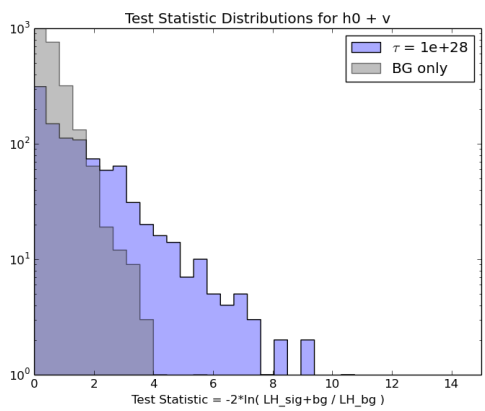

(c) $h^0\nu$ TS distribution for $\tau = 10^{28.0}$ s

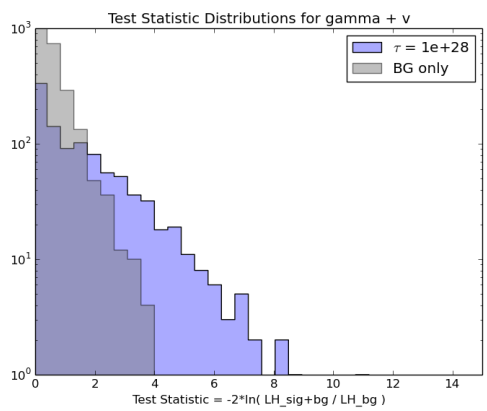

(d) $\gamma\nu$ TS distribution for $\tau = 10^{28.0}$ s

Decay Mode	**Best Fit DM Lifetime**	**Best Fit Astro Index**	**Sensitivity**
$W^+\tau^-$	$10^{28.0}$ s	-2.32	$10^{27.95}$ s
$Z^0\nu$	$10^{28.0}$ s	-2.37	$10^{28.0}$ s
$h^0\nu$	$10^{28.1}$ s	-2.31	$10^{28.0}$ s
$\gamma\nu$	$10^{28.1}$ s	-2.31	$10^{28.0}$ s

Fig. 5.8.: LLH1 Test Statistic Distributions for 2 PeV DM decay modes corresponding to 90% CL sensitivity.

distributions and corresponding sensitivities are show in Figure 5.11 for a sample decay mode ($W^+\tau^-$) using Likelihood method 1.

5.3.7 Effects of More Pseudoexperiments

The sensitivities reported in this analysis used 10000 pseudoexperiments generated from background-only sources. Figure 5.12 shows the effect of increasing the number of

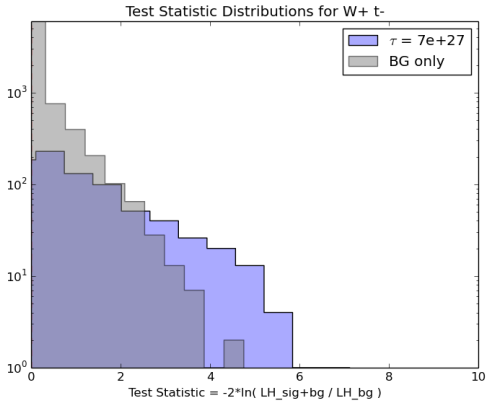

(a) $W^+\tau^-$ TS distribution for $\tau = 10^{27.85}$ s

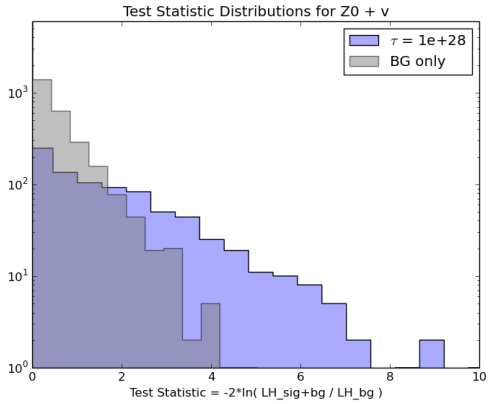

(b) $Z^0\nu$ TS distribution for $\tau = 10^{28.0}$ s

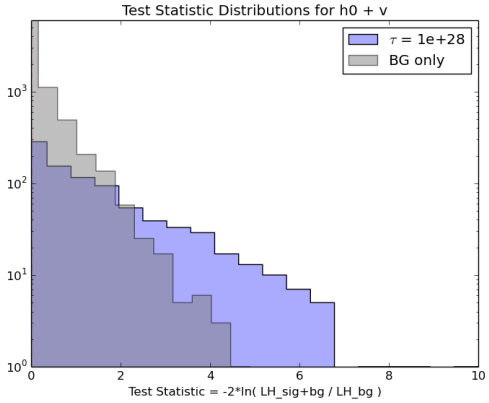

(c) $h^0\nu$ TS distribution for $\tau = 10^{28.0}$ s

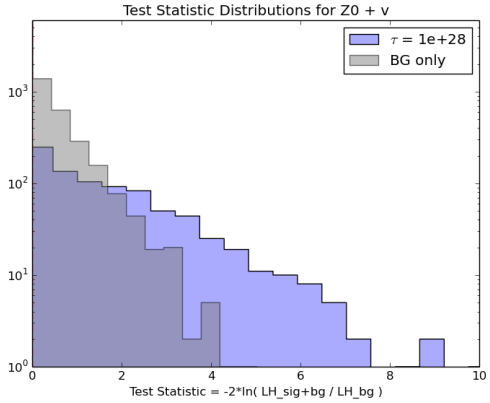

(d) $\gamma\nu$ TS distribution for $\tau = 10^{28.0}$ s

Decay Mode	BF DM Lifetime	BF Astro Index	BF Astro Norm	Sensitivity
$W^+\tau^-$	$10^{27.84}$ s	-2.94	0.26	$10^{27.85}$ s
$Z^0\nu$	$10^{27.99}$ s	-3.24	3.71	$10^{28.0}$ s
$h^0\nu$	$10^{27.96}$ s	-2.94	1.63	$10^{28.0}$ s
$\gamma\nu$	$10^{28.13}$ s	-3.08	4.05	$10^{28.0}$ s

Fig. 5.9.: LLH2 Test Statistic Distributions for 2 PeV DM decay modes corresponding to 90% CL sensitivity.

pseudoexperiments for bg only from 1000 to 10000 for the LLH method 1. The effect of this increase was minimal, but was implemented for all likelihood methods in order to increase the robustness of the analysis.

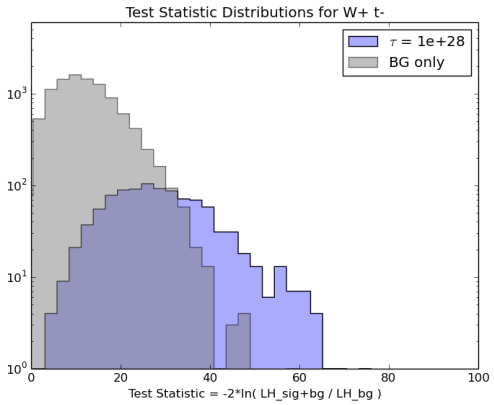

(a) $W^+\tau^-$ TS distribution for $\tau = 10^{28.0}$ s

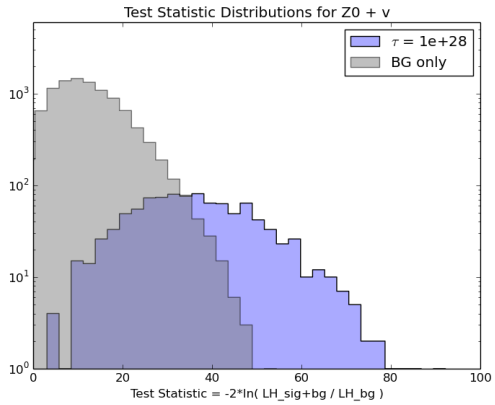

(b) $Z^0\nu$ TS distribution for $\tau = 10^{28.3}$ s

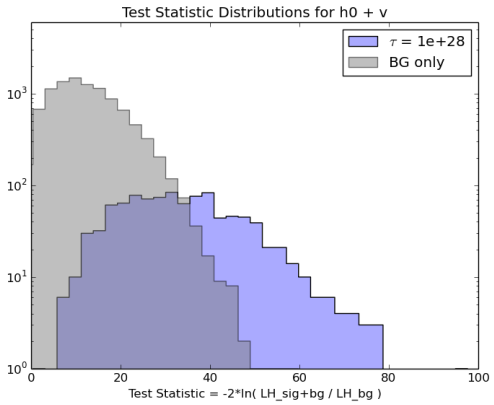

(c) $h^0\nu$ TS distribution for $\tau = 10^{28.3}$ s

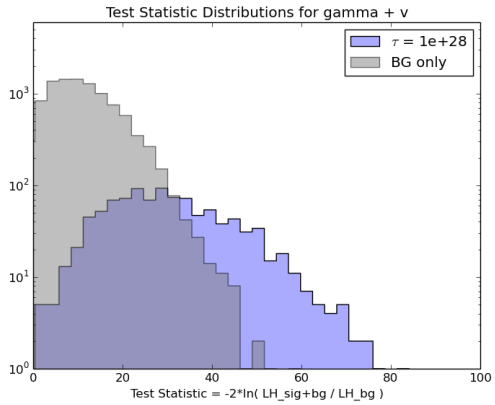

(d) $\gamma\nu$ TS distribution for $\tau = 10^{28.3}$ s

Decay Mode	**BF DM Lifetime**	**Sensitivity**
$W^+\tau^-$	$10^{27.62}$ s	$10^{28.0}$ s
$Z^0\nu$	$10^{27.66}$ s	$10^{28.3}$ s
$h^0\nu$	$10^{27.64}$ s	$10^{28.3}$ s
$\gamma\nu$	$10^{27.61}$ s	$10^{28.3}$ s

Fig. 5.10.: LLH3 Test Statistic Distributions for 2 PeV DM decay modes corresponding to 90% CL sensitivity.

5.3.8 Effects of Removing Tracks

To separate tracks and cascades, the log-likelihood ratio (log(track likelihood) - log(cascade likelihood)) was used to characterize an event as "track-like" or "cascade-like", with the most positive values representing events that were clearly cascade-like. The simulated distribution of the llhratio for 2 PeV DM events passing the HESE veto is shown in Figure 5.13.

The first attempt at removing tracks naively cut out events with an llhratio below 0, meaning they were more track-like than cascade-like. This proved to be too strong of

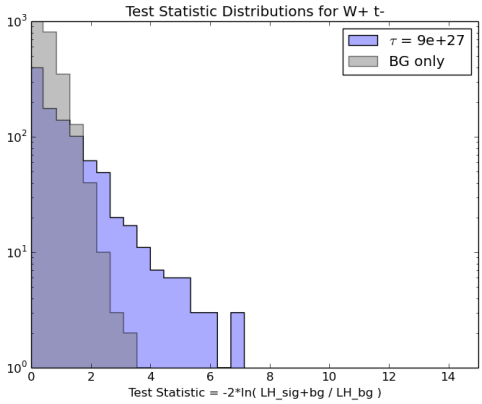

(a) Bin sizes equal to mean resolution (91% sig+bg above bg only)

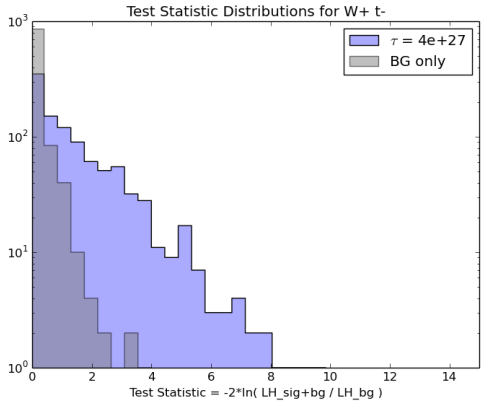

(b) Twice as many bins (90.3% sig+bg above bg only)

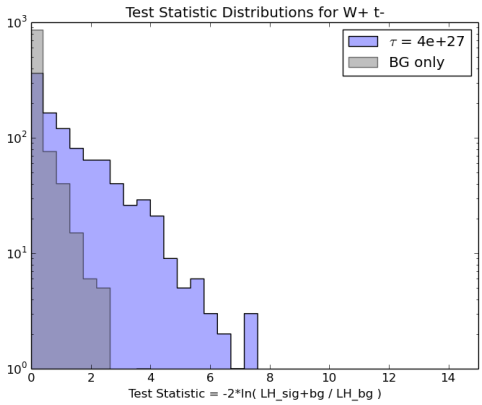

(c) Half as many bins (91% sig+bg above bg only)

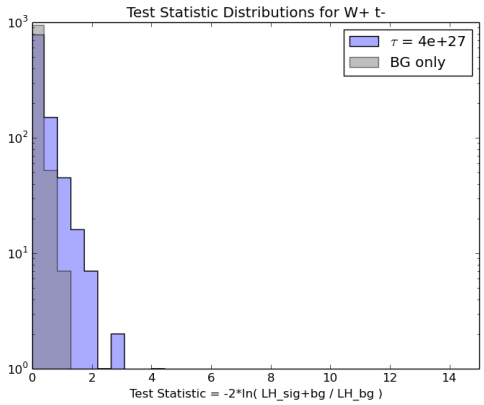

(d) 2x2 binning (69% sig+bg above bg only)

Fig. 5.11.: Effects of binning on $W^+\tau^-$ channel for LLH method 1.

a cut, and negatively affected the sensitivity. This meant that softer cuts needed to be analyzed. The effect of each cut on the reconstructed energy, as well as the sensitivities (for LLH method 1) are shown in Tables 5.4 and 5.5 respectively.

The idea of removing tracks from the event sample was due to their possible negative impact on the energy resolution. Since the energy distribution is the most important aspect for identifying a spectral line feature, it was thought that including tracks might hurt the sensitivity of the analysis. To understand this impact, I cut on the Monte Carlo truth and removed all tracks (ν_μ CC-interactions) from the sample. The resulting sensitivity is shown

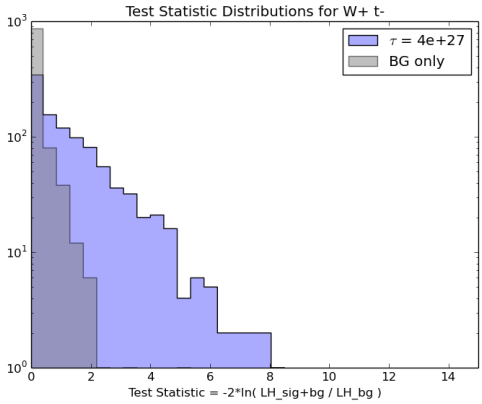

(a) $W^+\tau^-$ sensitivity did not change

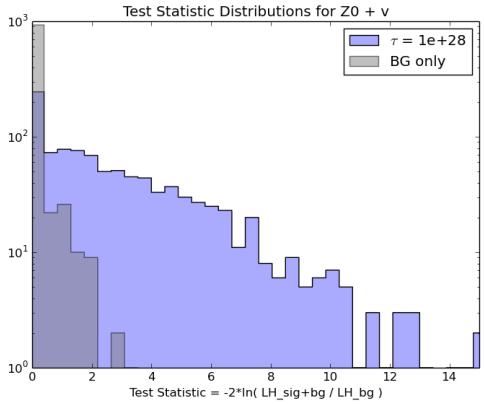

(b) $Z^0\nu$ sensitivity increased from 92 to 94 percent above

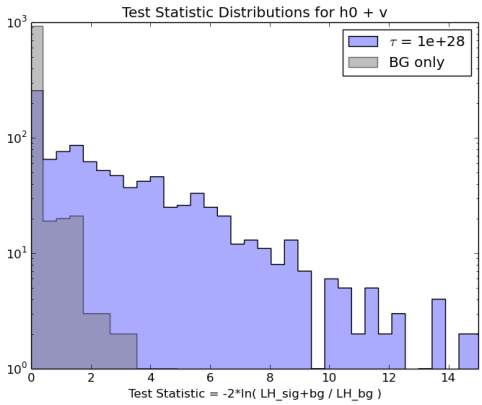

(c) $h^0\nu$ sensitivity increased from 92 to 93 percent above

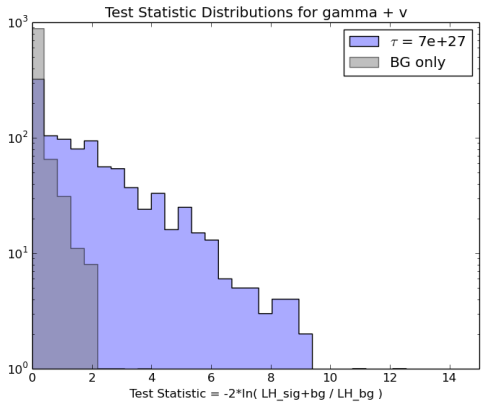

(d) $\gamma^0\nu$ sensitivity did not change

Fig. 5.12.: Effects of more pseudoexperiments on each decay mode for LLH method 1.

below, and is actually slightly worse. This is likely due to the removal of cascade-like tracks, for which the cascade reconstruction can accurately estimate the energy. Ultimately, the decision was made not to attempt to remove tracks from the final sample due to the lack of improvement to the reconstruction and the negative effect on the sensitivity.

5.3.9 Effect of Halo Profile

For a decay analysis, the resulting flux is only mildly sensitive to the choice of halo profile (Figure 5.14). The analysis was performed with Burkert and NFW profiles and the sensitivities only slightly improved for the more cuspy NFW profile (Figure 5.7. Since the Burkert profile better fits with observations, including the Milky Way [22], the Burkert profile was chosen for this analysis.

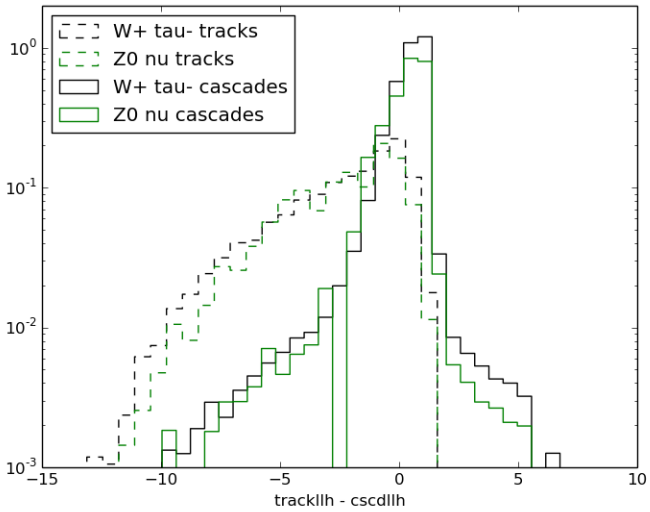

Fig. 5.13.: Log-likelihood ratios (trackllh - cscdllh) for simulated 2 PeV DM events passing the HESE veto. Positive numbers indicate cascade-like events, while negative numbers represent events that were more track-like.

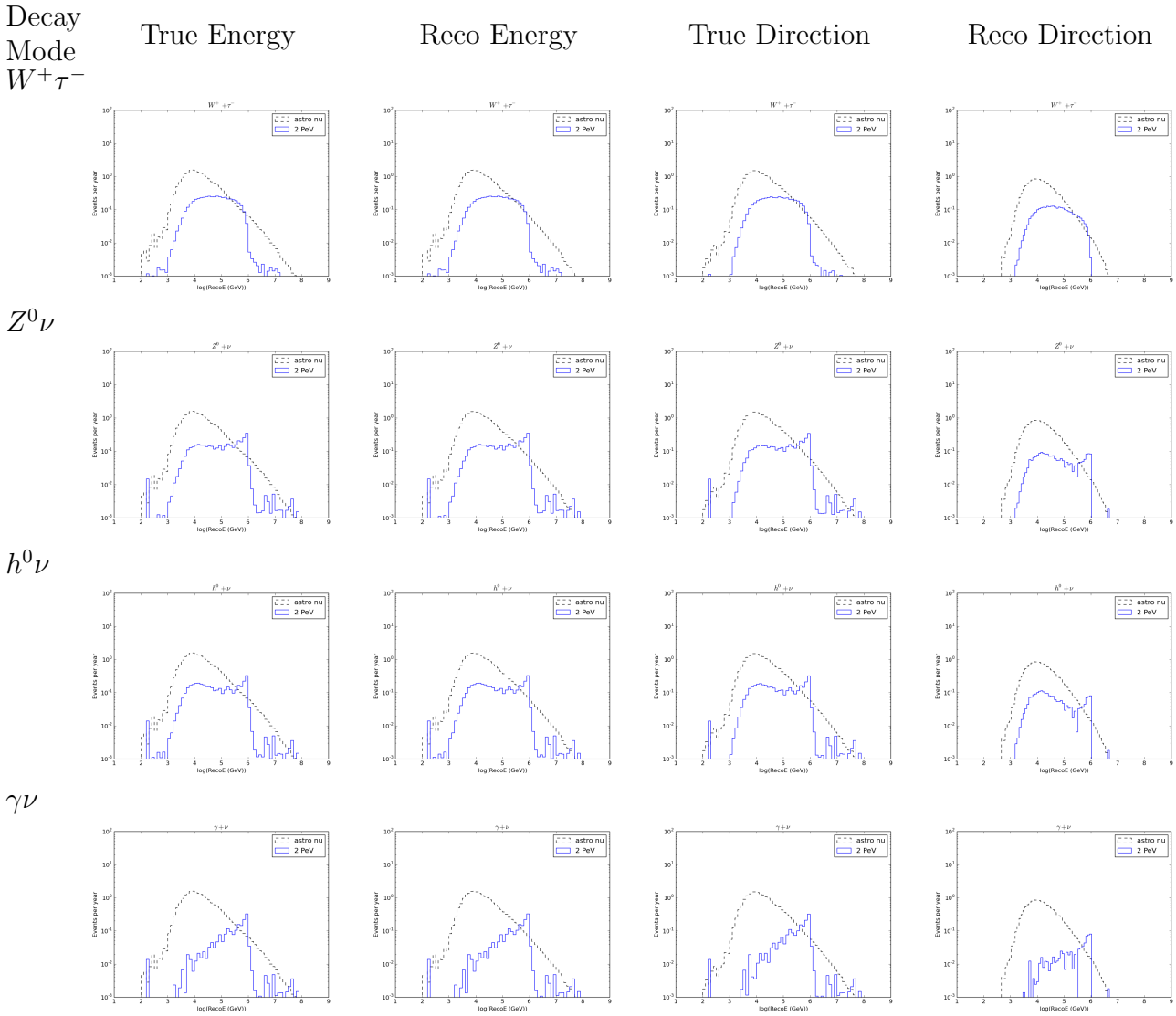

Table 5.4.: Reconstructed energy studies as a function of cutting on the llhratio in an attempt to remove tracks. Removal of tracks did not significantly improve the reconstruction resolution and had a negative impact on the sensitivity, and therefore was not implemented in the final analysis.

Decay Mode	**None**	**>-15**	**>-5**	**>0**
$W^+\tau^-$	$10^{27.78}$ s	$10^{27.78}$ s	$10^{27.78}$ s	$10^{27.70}$ s
$Z^0\nu$	$10^{27.95}$ s	$10^{27.95}$ s	$10^{27.95}$ s	$10^{27.60}$ s
$h^0\nu$	$10^{27.85}$ s	$10^{27.85}$ s	$10^{27.90}$ s	$10^{27.50}$ s
$\gamma\nu$	$10^{27.90}$ s	$10^{27.90}$ s	$10^{27.90}$ s	$10^{27.50}$ s

Table 5.5.: Sensitivity for each decay mode as a function of a cut on the LLH ratio.

Decay Mode	All Events	Cascades Only
$W^+\tau^-$	$10^{27.78}$ s	$10^{27.70}$ s
$Z^0\nu$	$10^{27.95}$ s	$10^{27.85}$ s
$h^0\nu$	$10^{27.85}$ s	$10^{27.78}$ s
$\gamma\nu$	$10^{27.90}$ s	$10^{27.78}$ s

Table 5.6.: Effect of removing cascades on the LLH1 sensitivity

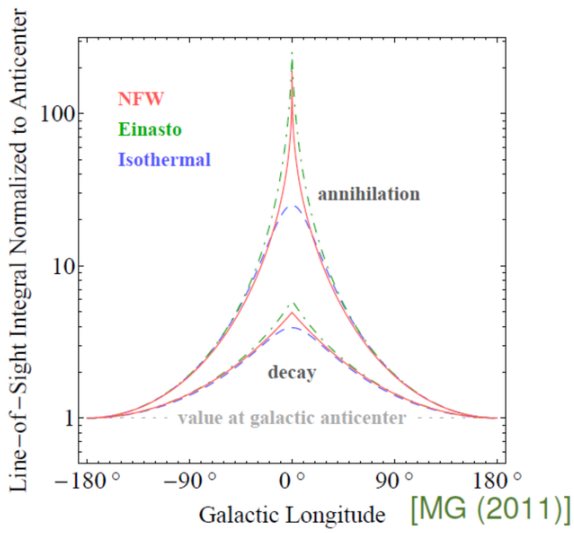

Fig. 5.14.: Plot showing the line of sight integral for decay analysis and various halo profiles (M. Grefe 2011).

Decay Mode	Burkert	NFW
$W^+\tau^-$	$10^{27.79}$ s	$10^{27.79}$ s
$Z^0\nu$	$10^{27.95}$ s	$10^{28.0}$ s
$h^0\nu$	$10^{27.90}$ s	$10^{28.0}$ s
$\gamma\nu$	$10^{27.90}$ s	$10^{28.0}$ s

Table 5.7.: Sensitivity of LLH1 for Burkert and NFW choices of halo profile.

6 RESULTS

After the analysis procedure was approved by the IceCube BSM group, one year of run data from IC86-2011 was analyzed. The passing events were histogrammed in the same way as the simulation data and are shown in Figure 6.1.

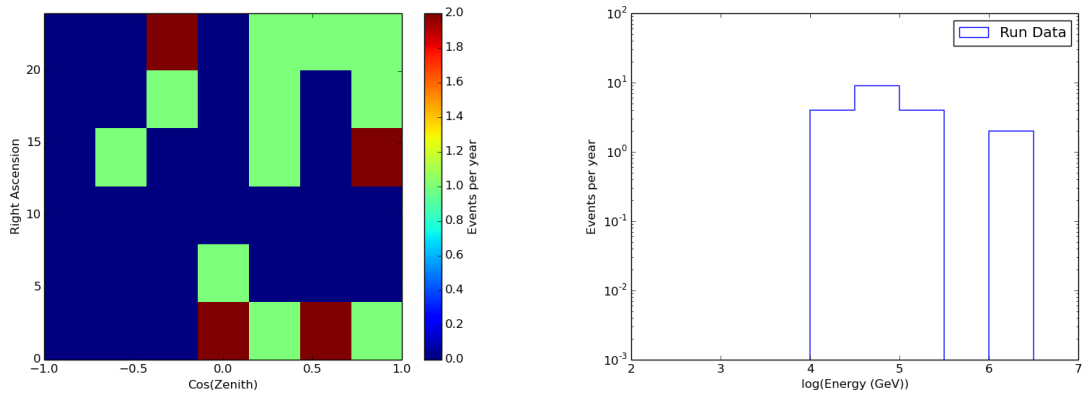

(a) (b)

Fig. 6.1.: Actual events from the run data binned according to the bin sizes used in the 3d fitter. The directional distribution (a) is integrated over all energies and shows events arriving from around the GC, as described in [44]. There are more downgoing events than upgoing due to absorption by the Earth. The energy distribution integrated over all arrival angles (b) shows a "gap" in the energy distribution and a peak corresponding to the two highest energy events in the 2011 data known as "Bert" and "Ernie".

In order to set a limit, the IC86-2011 run data were binned exactly the same as the pseudodata. The histogram was fit with background only sources, as well as signal + background, and a test statistic was calculated for each decay mode for each likelihood method. The 90% CL sensitivity was determined by which dark matter lifetime had 90% of the TS distribution above the median of the background. For setting a limit, the same procedure was followed, but using the TS value from the data. The dark matter lifetime with 90% of its TS distribution above the run data TS represents the limit at 90% CL.

Figure 6.2 shows the TS distributions with the median of the background-only distribution labeled as well as the TS calculated from the data for the $\gamma\nu$ channel. The median of the background and data TS were very consistent with the background-only hypothesis for LLH1 and LLH2 and thus appear to the far left of the plot. For LLH3, the number of events in the data are well above what was predicted by the purely atmospheric background, and therefore the data TS is much higher than the median of the background-only distribution. Ultimately, this results in a worse limit due to the fact that shorter DM lifetimes cannot be ruled out. Actual limits on the DM lifetime are shown in Figure 6.1 for each decay mode for all likelihood methods. This analysis marks the first limit on the gravitino lifetime by IceCube, and is within the range predicted by limits based solely on the IceCube published data assuming only an atmospheric background, as in [85].

Decay Mode	**LLH1 Limit**	**LLH2 Limit**	**LLH3 Limit**
$W^+\tau^-$	$10^{27.85}$ s	$10^{27.78}$ s	$10^{27.60}$ s
$Z^0\nu$	$10^{27.95}$ s	$10^{27.90}$ s	$10^{27.69}$ s
$h^0\nu$	$10^{27.95}$ s	$10^{27.90}$ s	$10^{27.69}$ s
$\gamma\nu$	$10^{27.95}$ s	$10^{27.90}$ s	$10^{27.69}$ s

Table 6.1.: Limits on the DM Lifetime for LLH1-3

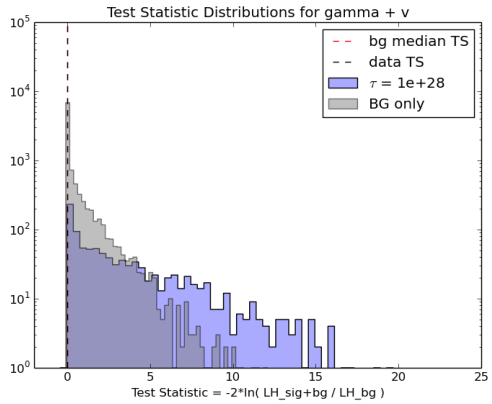

(a) LLH1

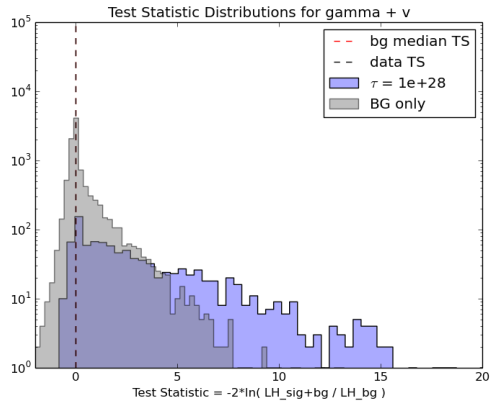

(b) LLH2

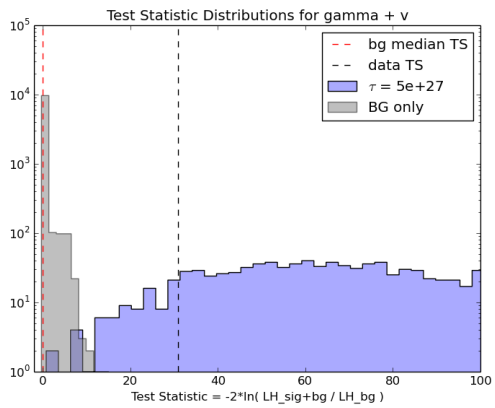

(c) LLH3

Fig. 6.2.: Test statistic distributions for all likelihoods showing the location of the median of the background-only distributions as well as the value of the test statistic calculated from the IC86-2011 run data. For LLH1 and LLH2 the data were very consistent with background and thus the data TS falls almost exactly on the median of the bg line.

6.1 Cut and Count Limits

Due to the unique energy spectrum and arrival direction, a likelihood analysis was expected to outperform a simple cut and count, where the number of neutrino events that passed the veto were compared to the expected number of background events as described in [86],

$$\Phi(E,\theta)_{90\%} = \Phi(E,\theta)\frac{\mu_{90}(n_{obs}, n_b)}{n_s} \tag{6.1}$$

where $\Phi(E,\theta)_{90\%}$ is the 90% CL limit on the flux, $\Phi(E,\theta)$ is the predicted flux, μ_{90} is the Feldman-Cousins limit from [86] which is a function of the number of observed events (n_{obs}) and the number of expected background events (n_b), and the number of expected signal events (n_s).

The limits shown in Table 6.2 correspond to the cut-and-count procedure, and as expected, rule out shorter lifetimes than the likelihood analyses. This is due to the fact that the cut-and-count method neglects the shape of the energy spectrum and arrival direction. The background can vary significantly in the second likelihood method, so cut-and-count sensitivities are only listed for the first method, using the published power law fit, and the third method where the only background is the atmospheric flux. Due to the sensitivities being solely a function of the total number of neutrinos, the line spectra do not necessarily have an advantage over the softer $W\tau$ channel. This affect is most noticeable for the $\gamma\nu$ channel which produces the least number of neutrinos. As reconstruction algorithms and computer hardware improve, and if IceCube commissions new infill strings, energy and direction sensitivity should improve enough to increase the number of bins used for this likelihood analysis, and thereby increase the performance of the likelihood method versus cut-and-count.

Decay Mode	**LLH1**	**LLH3**
$W^+\tau^-$	$10^{27.65}$s	$10^{27.41}$s
$Z^0\nu$	$10^{27.65}$s	$10^{27.41}$s
$h^0\nu$	$10^{27.59}$s	$10^{27.35}$s
$\gamma^0\nu$	$10^{27.50}$s	$10^{27.26}$s

Table 6.2.: Cut and count limits for the first and third likelihood methods.

7 CONCLUSION

The decay of very heavy dark matter is an interesting hypothesis of the recently observed flux of high-energy neutrinos by IceCube. Although the observed neutrinos could have been produced by conventional astrophysical sources (such as AGN or GRBs), gravitinos are a well motivated candidate for heavy dark matter and can have high enough energies to produce the neutrinos observed by IceCube. This analysis studied the gravitino dark matter decay scenario via a maximum likelihood method, taking into account the energy and arrival direction of events, and set limits on the dark matter lifetime for the two-body decay modes. More statistics are necessary to distinguish between the dark matter and astrophysical hypotheses.

This analysis uses a frequentist method of setting limits, which precluded making a statement about detection. This choice was made due to time constraints and the computational complexity of using the Feldman-Cousins method (described in [86]), which transitions seamlessly from an upper limit to a central limit. The next step for this analysis will be to extend the limits on the gravitino lifetime to DM masses in the PeV - 10 PeV range, using four years of IceCube data.

This analysis marks the first IceCube dark matter search involving gravitinos, as well as a spectral line. The gravitino spectra generated with PYTHIA, along with the techniques developed herein, will be used in future analyses to search for gravitino dark matter. With the completion of the promising $m_{DM} = 2$ PeV search, this analysis can be easily extended to cover a larger range of masses. Future searches will extend this limit to a wider mass range as well as incorporate more detector livetime and other event selections, and thus improve the limits. With promising extensions to IceCube on the horizon, such as the High Energy Extension, IceCube will play a prominent role in future searches for

very heavy dark matter candidates.

8 REFERENCES

[1] D. Kazakov, Phys. Usp. **57**, 930 (2014), 1405.5495, [Usp. Fiz. Nauk184,no.9,1004(2014)].

[2] ATLAS, G. Aad *et al.*, Phys. Lett. **B716**, 1 (2012), 1207.7214.

[3] CMS, S. Chatrchyan *et al.*, Phys. Lett. **B716**, 30 (2012), 1207.7235.

[4] E. Fermi, Il Nuovo Cimento (1924-1942) **11**, 1 (2008).

[5] C. L. Cowan, F. Reines, F. B. Harrison, H. W. Kruse, and A. D. McGuire, Science **124**, 103 (1956).

[6] G. Danby *et al.*, Phys. Rev. Lett. **9**, 36 (1962).

[7] M. L. Perl *et al.*, Phys. Rev. Lett. **35**, 1489 (1975).

[8] DONUT, K. Kodama *et al.*, Phys. Lett. **B504**, 218 (2001), hep-ex/0012035.

[9] R. Davis, D. S. Harmer, and K. C. Hoffman, Phys. Rev. Lett. **20**, 1205 (1968).

[10] B. Pontecorvo, Sov. Phys. JETP **6**, 429 (1957), [Zh. Eksp. Teor. Fiz.33,549(1957)].

[11] SNO Collaboration, Q. R. Ahmad *et al.*, Phys. Rev. Lett. **87**, 071301 (2001).

[12] J. Kopp, *Phenomenology of Three-Flavour Neutrino Oscillations*, PhD thesis, Technische Universitt Mnchen, 2006.

[13] Particle Data Group, K. A. Olive *et al.*, Chin. Phys. **C38**, 090001 (2014).

[14] C. Rovelli, Notes for a brief history of quantum gravity, in *Recent developments in theoretical and experimental general relativity, gravitation and relativistic field theories. Proceedings, 9th Marcel Grossmann Meeting, MG'9, Rome, Italy, July 2-8, 2000. Pts. A-C*, pp. 742–768, 2000, gr-qc/0006061.

[15] S. Weinberg, Phys. Rev. **138**, B988 (1965).

[16] LIGO Scientific Collaboration and Virgo Collaboration, B. P. Abbott *et al.*, Phys. Rev. Lett. **116**, 061102 (2016).

[17] C. M. Will, Phys. Rev. D **57**, 2061 (1998).

[18] F. Zwicky, Helv. Phys. Acta **6**, 110 (1933), [Gen. Rel. Grav.41,207(2009)].

[19] V. C. Rubin, N. Thonnard, and W. K. Ford, Jr., Astrophys. J. **238**, 471 (1980).

[20] W. J. G. de Blok, (2009), arXiv:0910.3538.

[21] J. F. Navarro, C. S. Frenk, and S. D. M. White, ApJ**462**, 563 (1996), astro-ph/9508025.

[22] F. Nesti and P. Salucci, jcap **7**, 016 (2013), 1304.5127.

[23] R. A. Alpher, H. Bethe, and G. Gamow, Phys. Rev. **73**, 803 (1948).

[24] B. D. Fields, K. Freese, and D. S. Graff, Astrophys. J. **534**, 265 (2000), astro-ph/9904291.

[25] K. Freese, B. Fields, and D. Graff, Nucl. Phys. Proc. Suppl. **80**, 0305 (2000), astro-ph/9904401.

[26] M. Milgrom, The Astrophysical Journal **270**, 365 (1983).

[27] V. Springel *et al.*, Nature **435**, 629 (2005), astro-ph/0504097.

[28] R. D. Peccei and H. R. Quinn, Phys. Rev. Lett. **38**, 1440 (1977).

[29] S. M. Bilenky and C. Giunti, Int. J. Mod. Phys. **A16**, 3931 (2001), hep-ph/0102320.

[30] A. Kusenko, Phys. Rept. **481**, 1 (2009), 0906.2968.

[31] A. Pontzen and F. Governato, Nature**506**, 171 (2014), 1402.1764.

[32] R. Adhikari *et al.*, Submitted to: White paper (2016), 1602.04816.

[33] G. Jungman, M. Kamionkowski, and K. Griest, Phys. Rept. **267**, 195 (1996), hep-ph/9506380.

[34] M. Kamionkowski, WIMP and axion dark matter, in *High-energy physics and cosmology. Proceedings, Summer School, Trieste, Italy, June 2-July 4, 1997*, pp. 394–411, 1997, hep-ph/9710467.

[35] G. R. Farrar and P. Fayet, Physics Letters B **76**, 575 (1978).

[36] M. Grefe, ArXiv e-prints (2011), 1111.6041.

[37] M. Grefe, *Unstable Gravitino Dark Matter - Prospects for Indirect and Direct Detection*, PhD thesis, Hamburg U., 2011, 1111.6779.

[38] A. Esmaili and P. D. Serpico, (2013), arXiv:1308.1105.

[39] A. Esmaili, S. K. Kang, and P. D. Serpico, (2014), arXiv:1410.5979.

[40] B. Feldstein, A. Kusenko, S. Matsumoto, and T. T. Yanagida, (2013), arXiv:1303.7320.

[41] J. Kopp, J. Liu, and X.-P. Wang, (2015), arXiv:1503.02669.

[42] J. Zavala, (2014), arXiv:1404.2932.

[43] IceCube Collaboration, Science **342**, 1242856 (2013), 1311.5238.

[44] M. G. Aartsen *et al.*, Physical Review Letters **113**, 101101 (2014), 1405.5303.

[45] R. Abbasi *et al.*, Nuclear Instruments and Methods in Physics Research A **700**, 188 (2013), 1207.6326.

[46] R. Abbasi *et al.*, Astroparticle Physics **35**, 615 (2012), 1109.6096.

[47] V. Ginis and P. Tassin, Philosophical Transactions of the Royal Society of London A: Mathematical, Physical and Engineering Sciences **373** (2015), http://rsta.royalsocietypublishing.org/content/373/2049/20140361.full.pdf.

[48] R. Abbasi *et al.*, Nuclear Instruments and Methods in Physics Research A **618**, 139 (2010), 1002.2442.

[49] IceCube, R. Abbasi *et al.*, Nucl. Instrum. Meth. **A601**, 294 (2009), 0810.4930.

[50] The IceCube Collaboration, ArXiv e-prints (2008), 0810.4930.

[51] IceCube, A. Achterberg *et al.*, Astropart. Phys. **26**, 155 (2006), astro-ph/0604450.

[52] T. I. Collaboration *et al.*, (2010), arXiv:1002.2442.

[53] F. Halzen and S. R. Klein, Rev. Sci. Instrum. **81**, 081101 (2010), 1007.1247.

[54] Into the Ice: Completing the IceCube Neutrino Observatory. https://newscenter.lbl.gov/2010/12/17/completing-icecube/, Accessed: 2016-10-30.

[55] World's largest particle detector icecube detects first high-energy neutrinos from the cosmos. http://phys.org/news/2013-11-world-largest-particle-detector-icecube.html, Accessed: 2016-10-30.

[56] IceCube, M. G. Aartsen *et al.*, JINST **9**, P03009 (2014), 1311.4767.

[57] S. L. Glashow, Phys. Rev. **118**, 316 (1960).

[58] IceCube, M. G. Aartsen *et al.*, Phys. Rev. **D88**, 112008 (2013), 1310.5477.

[59] A. E. Brenner *et al.*, Phys. Rev. D **26**, 1497 (1982).

[60] IceCube, M. G. Aartsen *et al.*, Phys. Rev. **D89**, 062007 (2014), 1311.7048.

[61] IceCube, M. G. Aartsen *et al.*, Eur. Phys. J. **C75**, 116 (2015), 1409.4535.

[62] M. Honda, T. Kajita, K. Kasahara, S. Midorikawa, and T. Sanuki, Phys. Rev. **D75**,

043006 (2007), astro-ph/0611418.

[63] T. K. Gaisser, Astropart. Phys. **35**, 801 (2012), 1111.6675.

[64] Los Alamos Science 25 (1997). http://permalink.lanl.gov/object/tr?what=info:lanl-repo/lareport/LA-UR-97-2534-03 , Accessed: 2016-10-30.

[65] IceCube, A. Schukraft, Nucl. Phys. Proc. Suppl. **237-238**, 266 (2013), 1302.0127.

[66] R. Enberg, M. H. Reno, and I. Sarcevic, Phys. Rev. **D78**, 043005 (2008), 0806.0418.

[67] IceCube, M. G. Aartsen *et al.*, Eur. Phys. J. **C75**, 116 (2015), 1409.4535.

[68] IceCube, M. G. Aartsen *et al.*, Nucl. Instrum. Meth. **A711**, 73 (2013), 1301.5361.

[69] IceCube, M. G. Aartsen *et al.*, The IceCube Neutrino Observatory Part VI: Ice Properties, Reconstruction and Future Developments, in *Proceedings, 33rd International Cosmic Ray Conference (ICRC2013): Rio de Janeiro, Brazil, July 2-9, 2013*, 2013, 1309.7010.

[70] J. K. Becker, Phys. Rept. **458**, 173 (2008), 0710.1557.

[71] IceCube Collaboration, M. G. Aartsen *et al.*, Phys. Rev. Lett. **115**, 081102 (2015).

[72] D. Heck, G. Schatz, T. Thouw, J. Knapp, and J. N. Capdevielle, (1998).

[73] A. Gazizov and M. P. Kowalski, Comput. Phys. Commun. **172**, 203 (2005), astro-ph/0406439.

[74] D. Xu, *Search for Astrophysical Tau Neutrinos in Three Years of IceCube Data*, PhD thesis, University of Alabama, 2015.

[75] M. Larson, Simulation and Identification of Non-Poissonian Noise Triggers in the IceCube Neutrino Detector, Master's thesis, University of Alabama, 2013.

[76] IceCube, M. G. Aartsen *et al.*, Phys. Rev. Lett. **114**, 171102 (2015), 1502.03376.

[77] R. Gandhi, C. Quigg, M. H. Reno, and I. Sarcevic, Astropart. Phys. **5**, 81 (1996), hep-ph/9512364.

[78] A. Cooper-Sarkar and S. Sarkar, Journal of High Energy Physics **1**, 075 (2008), 0710.5303.

[79] J. Lundberg *et al.*, Nuclear Instruments and Methods in Physics Research A **581**, 619 (2007), astro-ph/0702108.

[80] GEANT4, S. Agostinelli *et al.*, Nucl. Instrum. Meth. **A506**, 250 (2003).

[81] J. Ahrens *et al.*, Nuclear Instruments and Methods in Physics Research A **524**, 169

(2004), astro-ph/0407044.

[82] D. Pandel, *Bestimmung von Wasser und Detektorparametern und Rekonstruktion von Myonen bis 100 TeV mit dem Baikal-Neutrinoteleskop NT-72*, PhD thesis, 1996.

[83] A. Burkert, IAU Symp. **171**, 175 (1996), astro-ph/9504041, [Astrophys. J.447,L25(1995)].

[84] F. James and M. Roos, Comput. Phys. Commun. **10**, 343 (1975).

[85] C. Rott, K. Kohri, and S. C. Park, Phys. Rev. **D92**, 023529 (2015), 1408.4575.

[86] G. J. Feldman and R. D. Cousins, Phys. Rev. **D57**, 3873 (1998), physics/9711021.